Phytomedicine 140 (2025) 156586

Contents lists available at ScienceDirect

Phytomedicine

journal homepage: www.elsevier.com/locate/phymed

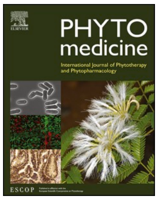

Original Article

Toosendanin-induced liver damage through irreparable DNA damage and autophagy flow blockade

Yifan Lin[a,b,1], Jian Zhang[a,b,1], Xinyue Gao[b,1], Zekai Wu[b], Lele Yang[b], Kun Tian[b], Xiaoqi Lv[c], Jiaqi Li[b], Kunqi Chen[b], Youbo Zhang[d], Hong Hu[a], An Zhu[a,b,*]

[a] *Fujian Provincial Key Laboratory of Environmental Factors and Cancer, School of Public Health, Fujian Medical University, Fuzhou, 350122, China*
[b] *Key Laboratory of Gastrointestinal Cancer (Fujian Medical University), Ministry of Education, Fuzhou, 350108, Fujian, China*
[c] *Key Laboratory of Cell Proliferation and Differentiation of the Ministry of Education, Peking University Genome Editing Research Center, College of Life Sciences, Peking University, Beijing, 100091, China*
[d] *State key laboratory of Natural and Biomimetic Drugs, and Department of Natural Medicines, School of Pharmaceutical Sciences, Peking University, Beijing, 100191, China*

ARTICLE INFO

Keywords:
Toosendanin
DNA damage responses
Cell cycle
Hepatotoxicity

ABSTRACT

Objective: The fruit of *Melia toosendan* Sieb. et Zucc. (MT) is known for its efficacy in relieving pain and treating roundworms. Toosendanin (TO) has been identified as a bioactive marker of MT, with hepatotoxic properties. This study offers a comprehensive investigation into the toxic mechanisms, involving TO-induced remaining DNA damage, cell cycle arrest, and the synergistic effect of autophagy flow disruption. It provides new insights into the clinical applications of MT and TO.

Methods: TO was prepared at 50, 100, and 200 μM for a 48 h treatment of HepG2 cells, while zebrafish were administered at 50, 75, and 100 μM for 72 h. Transcriptomics and computational molecular simulations, including network pharmacology, molecular docking, and molecular dynamics simulation, were used for target prediction. Fluorescent probes, flow cytometry, quantitative real-time polymerase chain reaction, and western blotting were employed for mechanism verification.

Results: TO disrupted the balance between reactive oxygen species and cellular antioxidant defense, resulting in mitochondrial damage and repression of DNA-dependent protein kinase catalytic subunit. This led to the inability to repair DNA damage and caused cell cycle arrest in the G1/S phase. As shown in computational molecular simulations and transcriptomics analysis, the repression of damaged organelle removal through autophagy flow disruption resulted in excessive injury and hepatocyte death.

Conclusion: By impairing DNA damage responses (DDRs) and autophagy, TO causes unrepaired DNA damage, which disrupts cell cycle progression through complex interactions with cyclin proteins and tumour suppressor genes, ultimately contributing to hepatotoxicity.

Abbreviations

ALT	alanine transaminase
ANOVA	one-way analysis of variance
AST	aspartate transaminase
ATM	ataxia telangiectasia-mutated
ATR	ataxia telangiectasia and Rad3-related
BP	biological process
CC	cell component
CCCP	carbonyl cyanide 3-chlorophenylhydrazone
CDK2	cyclin-dependent kinase 2
CDS	coding sequences
CHEK1	checkpoint kinase 1
CHEK2	checkpoint kinase 2
DDRs	DNA damage responses
DL	drug-likeness
DNA-PK	DNA-dependent protein kinase
DNA-PKcs	DNA-dependent protein kinase catalytic subunit
DSBs	double-strand breaks
GO	gene ontology

---

[*] Correspondence author at: Key Laboratory of Gastrointestinal Cancer (Fujian Medical University), Ministry of Education, Fuzhou 350108, Fujian, China.
E-mail address: zhuan@fjmu.edu.cn (A. Zhu).

[1] Yifan Lin, Jian Zhang, and Xinyue Gao have contributed equally to this work.

https://doi.org/10.1016/j.phymed.2025.156586
Received 23 September 2024; Received in revised form 16 February 2025; Accepted 25 February 2025
Available online 27 February 2025

GSEA	gene set enrichment analysis
GSH	glutathione
hpf	post-fertilization
HPLC	high-performance liquid chromatography
HR	homologous recombination
IACUC	institutional animal protection and use committee
KEGG	kyoto encyclopedia of genes and genomes
MD	molecular dynamics
MDA	malondialdehyde
MF	molecular function
MT	fructus of *Melia toosendan* Sieb. et Zucc.
NHEJ	non-homologous end joining
OB	oral bioavailability
PHE	phenylalanine
PPI	protein-protein interaction
Rg	radius of gyration
RMSD	root-mean-square deviation
RMSF	root-mean-square deviation
ROS	reactive oxygen species
RT-qPCR	quantitative real-time polymerase chain reaction
SEM	standard error
SOD	superoxide dismutase
SPONGE	Simulation Package tOward Next GEneration
SSBs	single-strand breaks
TCM	traditional Chinese medicine
TO	toosendanin
γ-H2AX	phosphorylated H2AX

Introduction

Natural products are crucial sources of lead compounds for drug discovery (Atanasov et al., 2021). *Melia toosendan* Sieb. et Zucc., a traditional Chinese medicine (TCM) found in Hubei, Sichuan, and Guizhou provinces (Shao et al., 2020), is known for its efficacy in relieving pain and expelling roundworms (Chinese Pharmacopoeia Committee, 2020). In a clinical trial, toosendan tablets were administered to 1327 patients as ascaricides, achieving a 60.7 % elimination rate within 24 h (Chongqing Traditional Chinese Medicine Hospital, 1957). Toosendanin (TO, $C_{30}H_{38}O_{11}$, Mw =574.62) extracted from the bark and fruit of *Melia toosendan* Sieb. et Zucc. (MT) has been identified as a key bioactive marker component (Fan et al., 2021; Zhang et al., 2010). However, its clinical application is significantly limited by its hepatotoxicity, owing to the easy accumulation in the liver and higher concentrations compared with other tissues (Qi et al., 2008). Previous study has showed the toxic effect in metabolism and mitochondrial dysfunction, as evidenced by integrated proteomic, metabolomic, and biological analyses (Yan et al., 2019). Nonetheless, the specific molecular mechanisms underlying TO-induced hepatotoxicity remain unclear.

The activities of TO, including induction of autophagy or apoptosis (Zhang et al., 2022), enhancement of sensitivity to anti-cancer drugs (Wang et al., 2023), and inhibition of migration (Yang et al., 2021), have been well studied. However, the cell cycle arrest (Wang et al., 2015) was studied with unclear causation and target cyclins. Checkpoint-mediated cell cycle arrest, regulated by ataxia telangiectasia and Rad3-related (ATR) and ataxia relangiectasia-mutated (ATM) proteins, is essential for single-strand breaks (SSBs) and double-strand breaks (DSBs) to maintain genetic stability (Niida and Nakanishi, 2006). When DNA damage cannot be repaired, autophagy is activated to restore cellular balance by removing dysfunctional components (Juretschke and Beli, 2021). Previous studies have found that TO treatment can cause lysosomal dysfunction and irreparable damage, which is potentially linked to the downregulation of transcription factor EB (Luo et al., 2022). However, the effects of TO on upstream factors that regulate autophagy remain unknown.

Lu et al. (2016) showed that the physiological impact of TO could be linked to epigenetic modifications of RNA. The effects on miRNA and mRNA expression profiles were dose-dependent with exposure to 40 and 80 mg/kg TO. N6-methyladenosine (m6A), one of the most common modifications in eukaryotic mRNAs (Kadumuri and Janga, 2018; Tang et al., 2021), has been reported to occur at 0.1–1.79 % per major base in mammals (Jones et al., 2020). Furthermore, low levels of m6A can impair DNA damage responses (DDRs), leading to instability of DNA repair factors such as Rad51 and Xrcc (Fu et al., 2023). In this study, the potential mechanisms underlying TO-associated liver damage were explored, focusing on DNA damage, autophagy, and their relationship with m6A modifications.

Materials and methods

Reagents and instruments

The chemical structure of TO (Must Bio-Technology Co., Ltd., Chengdu, China) was determined using NMR (Fig. 1B and C) and was depicted in Fig. 1A. The purity of TO, found to be 98.31 % using high-performance liquid chromatography (HPLC) (Fig. 1D). Primary antibodies, including mTOR, p-mTOR, LC3, p62, GAPDH,DNA-PKcs, ATR, ATM, CHEK2, p53, p21, CDK2, cyclin E1, β-catenin, cyclin D1, and secondary antibodies were purchased from Proteintech (Wuhan, China). While the p15 was purchased from ABclonal (Wuhan, China). Primers were provided by Sangon Biotech (Shanghai, China). MTT was from MACKLIN (Shanghai, China). LDH assay kit, DNA gamage assay kit, calcein AM probe, mito-tracker red CMXRos probe, RIPA buffer containing phosphatase and protease inhibitors, and cell cycle and apoptosis analysis kit were provided by Beyotime (Shanghai, China). TRIzol reagent from Invitrogen (Carlsbad, CA, USA) was used. fluo-4 AM probe, JC-10 probe, DCFH-DA probe, and superoxide dismutase (SOD) activity assay kit were from Solarbio (Beijing, China). Glutathione (GSH) assay kit was provided using Abbkine Scientific (Wuhan, China). Cell malondialdehyde (MDA), alanine transaminase (ALT) and aspartate transaminase (AST) assay kit were purchased from Nanjing Jiancheng Bioengineering Institute (Nanjing, China). SYBR Green I was obtained from Accurate Biology (Hunan, China). Epizyme Biotech (Shanghai, China) provided BCA reagents. A microplate reader (BioTek, Santa Clara, CA, USA), a fluorescence microscope (Zeiss, Oberkochen, BW, Germany), an Amersham Imager 680 System (Cytiva, Marlborough, MA, USA), a stereo-microscope (SMZ1270, Nikon, Tokyo, Japan), and a FACSCanto II system (Becton, Dickinson and Company, Franklin Lakes, NJ, USA) were utilized in this article.

Cell culture

The human hepatic epithelial-like cells HepG2, which were purchased from the American Type Culture Collection (Manassas, VA, USA), were cultured in DMEM with 10 % fetal bovine serum. The culture conditions were maintained at 5 % CO_2 and 37 °C. TO at concentrations of 50, 100, and 200 μM was used to treat HepG2 cells for 48 h for further detection when the cell confluency reached 80 %.

Zebrafish treatment

Zebrafish larvae were used as an *in vivo* model due to their genomic similarity to humans, making them valuable for drug toxicology studies (Howe et al., 2013). Moreover, the low breeding costs, short reproductive cycles, high fecundity, and transparent embryos, which allow direct observation. The zebrafish were maintained under 14 h light and 10 h darkness at a controlled temperature of 28.5 °C. Both zebrafish *Tg* (*fabp10a: DsRed*) and wild type AB strains were purchased from the China Zebrafish Resources Center (Wuhan, China). Healthy and sexually mature female and male fish were placed in mating tanks, and zebrafish embryos were obtained the next morning and transferred to Danieaus' buffer (0.592 g $MgSO_4{\bullet}7H_2O$, 0.313 g KCl, 20.34 g NaCl, 7.12 g HEPES, 20 L H_2O, 0.850 g $Ca(NO_3)_2{\bullet}4H_2O$) for culture at 28 °C. Healthy

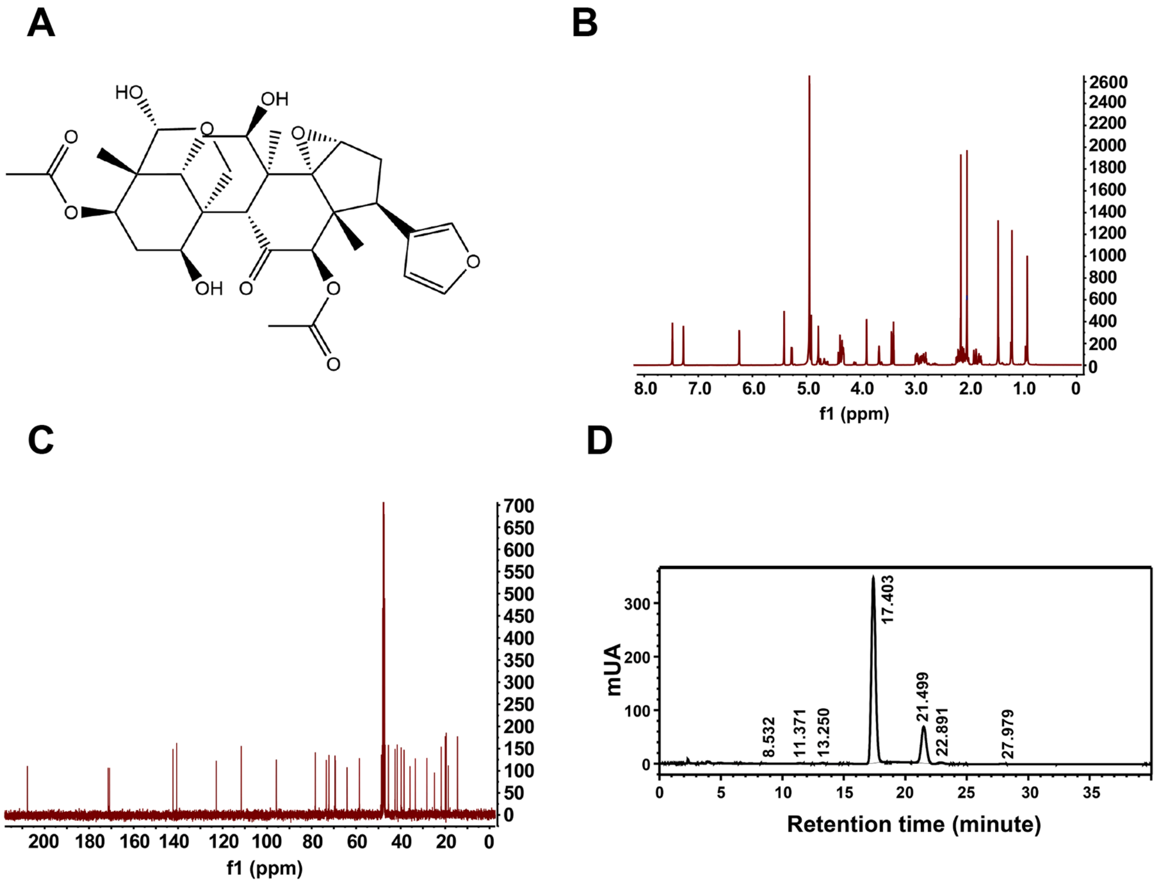

Fig. 1. Chemical structure. (A) Chemical construction of TO. (B) ^{1}H and (C) ^{13}C NMR spectra of TO. (D) HPLC analysis revealed that the purity of TO was 98.31 %, with retention times at 11.493 and 14.361 min.

zebrafish larvae at 72 h post-fertilization (hpf) were selected and transferred to 6-well plates, with 0, 50, 75, 100 μM of TO, respectively. The zebrafish larvae were cultured at 28.5 °C for 72 h. All operations adhered to the regulations of Institutional Animal Protection and Use Committee (IACUC) of Fujian Medical University (IACUC FJMU 2023-Y-0824, Mar 3, 2023).

Network pharmacology construction

Active components in MT

The active components of MT were screened using the TCM systems pharmacology database and analysis platform (TCMSP, https://old.tcmsp-e.com/) (Ru et al., 2014), with drug-likeness (DL) ≥0.18 and oral bioavailability (OB) ≥10 %. The SMILES strings of the potentially active components were obtained from PubChem (Li et al., 2010) and proceeded with the Swiss Target Prediction (Zoete et al., 2016).

Hepatotoxicity targets in MT

The keyword "liver toxicity" was entered into the GeneCards database, and genes with a relevance score above 10 were used. The overlap of MT active ingredient targets and liver toxicity genes was established using the VENNY2.1.0 website (http://www.liuxiaoyuyuan.cn/). DAVID database (Huang da et al., 2009) was used to analyse the kyoto encyclopedia of genes and genomes (KEGG) and gene ontology (GO) pathways of intersecting targets. The results were visualized and mapped using an online platform (https://www.bioinformatics.com.cn/).

Protein-protein interaction (PPI) network was constructed by uploading MT targets related to liver toxicity to the STRING database (Szklarczyk et al., 2023). Cytoscape 3.9.1 software (National Human Genome Research Institute, Bethesda, MD, USA) (Lopes et al., 2010) was used with the CytoNCA plug-in to screen the targets. Targets with a degree value ≥29 and their corresponding active ingredients were screened to construct the active ingredient-core target network (Li, 2021).

Molecular docking

The 3D structures of TO and the target proteins were downloaded from the PubChem (Lin et al., 2024) and PDB database (https://www.rcsb.org/) (Joosten et al., 2014), respectively. Compound molecules were pre-treated using SYBYL 2.0 software for energy minimisation, as well as hydrogenation and de-charging of target proteins, followed using semi-flexible docking of compounds to target proteins using a high-precision mode (Gao et al., 2020). The 3D structure of the complex was visualised using PyMol (Schrödinger, New York, NY, USA) (Lill and Danielson, 2011), and the protein-ligand complex was displayed using the 2D interaction mapping software LigPlot+ (European Molecular Biology Laboratory, Hinxton, Cambridgeshire, UK). Heatmaps of the docking scores for the compound-protein interactions were produced using the Hiplot website (https://hiplot.com.cn/).

Molecular dynamics (MD) simulations

MD simulations were employed to analyse affinity between the protein targets and TO. It was performed using Simulation Package tOward Next GEneration molecular modelling 1.3 software (SPONGE, Beijing, China) (Wu et al., 2024) with FF14SB Joint Atomic Force Field (Maier et al., 2015). The complex system was solved using the SPC/E water model (Linse and Hub, 2021) with the addition of K^{+} and Cl^{-} to neutralise the charges. Energy minimisation was performed *via* the steepest descent algorithm with a 5.0 kJ/mol tolerance. The system backbone atomic root-mean-square deviation (RMSD), root-mean-square deviation (RMSF), and radius of gyration (Rg), and binding free energy were analysed and then visualised using Origin 2021 (OriginLab, Northampton, MA, USA).

Detection of cell viability and LDH leakage

HepG2 cells were incubated with 0, 50, 100, 200, 400, 600, 800, and 1000 μM TO for 48 h in 96-well plates. A 10 μl MTT (MACKLIN) solution that dissolve in PBS was added to medium at 37 °C for 2 h. After aspirating the supernatant, DMSO was added to dissolve crystals for 10 min. Cell viability was quantified at 490 nm.

LDH leakage from cells was detected in 96-well plates after being exposed to 0, 50, 100, 200 μM TO for 48 h. Cell-free group, the untreated cell group, and the untreated cell group for subsequent lysis were set for calculation of LDH leakage as described in the manufacturer's instructions. Absorbance at 600 nm was measured after 30 min of incubation in the dark with reagent.

The m6A MeRIP-seq and mRNA-seq

HepG2 cells were co-cultured with 100 μM TO for 48 h and lysed using Trizol for total RNA extraction. To obtain 100–200 nt RNA fragments for m6A MeRIP-seq and mRNA-seq, 20mM $ZnCl_2$ was added. Sequencing procedures were performed by Seqhealth (Wuhan, China), using three separate samples per group. The stranded RNA sequencing library was constructed by incorporating unique molecular identifiers to mitigate duplication bias (Yu et al.,2024). Sequencing data were filtered by $|\log_2(\text{fold change})| > 0.263$, and $p < 0.05$, then uploaded to deepTools 2.4.1 (Ramírez et al., 2016), Homer 4.1 (Heinz et al., 2010), and David for analyses including m6A peak distribution, motif enrichment, GO, and KEGG enrichment.

Measurement of oxidative stress and calcium staining

ROS, GSH, SOD, and MDA level were used to assess oxidative stress in HepG2 cells treated with 0, 50, 100, and 200 μM TO for 48 h. ROS and GSH level were also evaluated *in vivo* at 50, 75, 100 μM for 72 h. Fluorescence microscope (Zeiss) was utilized for the purpose of observing and acquiring fluorescence micrographs of ROS. The levels of GSH, SOD, and MDA were measured at wavelengths of 412, 450, and 532 nm, respectively.

Additionally, calcium accumulation in HepG2 cells was detected using a fluo-4 AM probe. After adding 4 μM fluo-4 AM and incubating for 30 min, fluorescence was observed under a Zeiss microscope.

Quantification of DNA damage using γ-H2AX

γ-H2AX was used to quantify DNA damage in HepG2 cells incubated with 0, 50, 100, and 200 μM TO for 48 h in 24-well plates. The 0.03 % H_2O_2 was used as a positive control. The cells were incubated with γ-H2AX rabbit monoclonal antibody followed by a secondary antibody, and were subsequently examined under a Zeiss fluorescence microscope.

Detection of mPTP

The cells treated with 0, 50, 100, and 200 μM TO were exposed to calcein AM probe for 40 min to detect mitochondrial permeability transition pore (mPTP). Afterwards, the medium was replaced with the dye and incubated at 37 °C. The fluorescence microscope (Zeiss) was utilized for the purpose of observing and acquiring fluorescence micrographs.

Assessment of mitochondrial membrane potential (MMP)

HepG2 cells were processed as previously described and then incubated with JC-10 probe. Carbonyl cyanide 3-chlorophenylhydrazone (CCCP), an inhibitor of mitochondrial electron transport chain, acted as a positive control. Subsequently, the microscope (Zeiss) was utilized for the purpose of observing and acquiring fluorescence micrographs.

Assessing mitochondrial activity

HepG2 cells were processed accordingly and then incubated with 20 nM mito-tracker red CMXRos probe for 20 min. 0.03 % H_2O_2 was used as a positive control. Subsequently, the microscope (Zeiss) was utilized for the purpose of observing and acquiring fluorescence micrographs.

Real time quantitative reverse transcription polymerase chain reaction (RT-qPCR)

RNA extraction was described as before, followed by reverse transcription into cDNA, which was quantified to 1 μg/μl. A 20 μl reaction volume containing SYBR Green I was used for RT-qPCR on an IQ5 real-time PCR cycler. The relative gene expression under TO treatment with 0, 50, 100, 200 μM in HepG2 cells and 0, 50, 75, 100 μM in zebrafish larvae was quantified using the $2^{-\Delta\Delta Ct}$ method (Preston et al., 2020), with fold changes normalized against the control group. The *GAPDH* gene was employed as the internal control for mRNA. Table 1 provide the detailed primer sequences.

Western blotting

Following treatment with 0, 50, 100, 200 μM in HepG2 cells. The cell with RIPA lysate was subjected to ultrasonication, and then quantified to 1 μg/μl protein using BCA reagents (Epizyme Biotech). Equal quantities of proteins were separated and subsequently transferred to PVDF membranes at 300 mA. The membranes were incubated at room temperature with 5 % skimmed milk before being exposed to primary antibodies overnight. Afterward, the relative secondary antibody was applied. Images were visualized and quantified through Amersham Imager 680 System (Cytiva) and ImageJ software (Bio-Rad, Hercules, CA, USA), respectively.

Flow cytometry

The cell cycle and apoptosis analysis kit (Beyotime) was utilized for flow cytometry analysis after treating HepG2 cells with the 100 μM TO for 48 h. Samples were trypsinized without EDTA, washed with 1 ml PBS, and fixed in 70 % ethanol for 12 h. Finally, a 500 μl mixture of propidium iodide and RNase A was applied. The samples were analysed using FACSCanto II system (Becton) and visualised with FlowJo v10.8.1 software (Becton, Dickinson and Company).

Effect assessment of zebrafish exposed to TO

The survival rate of zebrafish larvae in each group was recorded by judging heartbeat after being subjected to 0, 50, 75, and 100 μM TO for 72 h. Fish in each group with spinal malformations or delayed yolk absorption was counted to obtain the malformation rate. The two experiments were repeated three times. The zebrafish larvae were photographed by fixing their lateral position. Body length of zebrafish larvae was measured using ImageJ software (Bio-Rad), and there were 15 replicates in each group. The Noldus DanioVision zebrafish tracking hardware system and Noldus EthoVision XT video tracking 10.1.856 software (Noldus Information Technology, Wageningen, Gelderland, Netherlands) were used to assess locomotor behavior of zebrafish larvae at 12-well plates. After the recording, the analysis examined locomotor distance, velocity, and duration over a duration of 5 min.

Fluorescence area of liver of zebrafish

Healthy zebrafish larvae were selected and treated in four concentration gradients as previously described. The zebrafish larvae were anesthetized with 0.02 % tricaine solution and photographed by fixing their lateral position. The fluorescence area of the liver of zebrafish larvae was observed using stereo-microscope (Nikon). Each group had 15 replicates.

Evaluation of ALT and AST of zebrafish

Zebrafish larvae after treatment were homogenized with physiological saline and centrifuged at 2500 × *g* for 10 min. The supernatant was retained to detect the activities of ALT and AST follow the manufacturer's instructions (Jiancheng Bioengineering Institute). The enzyme activities were calculated using absorbance at 510 or 505 nm.

Table 1

The sequences of RT-qPCR primers used for HepG2 cells and zebrafish larvae in this research.

Organism	Gene	Forward primer (5′→3′)	Reverse primer (5′→3′)
Homo sapiens	*mTOR*	GAGATACGCTGTCATCCCTTTA	CTGTATTATTGACGGCATGCTC
	LC3	GCCTTCTTCCTGCTGGTGAACC	TCCTCGTCTTTCTCCTGCTCGTAG
	p62	TGATTGAGTCCCTCTCCCAGATGC	CCGCTCCGATGTCATAGTTCTTGG
	DNA-PKcs	AGTGAGCCAGCCTGCCTTG	ACACCTTCTCTGAATCCTCTGAACTG
	ATM	GCTGTGGTGGAGGGAAGATGTTAC	CCTGCCTGGCGTGTTGATGAG
	ATR	CACCACCAGACAGCCTACAATGC	CCAGAGCCACTTTGCCCTTTCC
	CHEK1	CTGCCACATGATCGGACCATCG	GAGAATCGCTTGAACCCAGGAGAC
	CHEK2	CCAGCCAGTCCTCTCACTCCAG	GGTTCTTGGTCCTCAGGTTCTTGG
	p53	GCCCATCCTCACCATCATCACAC	GCACAAACACGCACCTCAAAGC
	p21	TCCAGCGACCTTCCTCATCCAC	TCCATAGCCTCTACTGCCACCATC
	CDK2	AGGATGTGACCAAGCCAGTACCC	CCACCTGAGTCCAAATAGCCCAAG
	cyclin E1	GATGGCATCAAACAGGGCAAAGTG	TGTCTGGAGGTGGCTGGTGTAC
	p15	GACTGGACCTGGTGGCTACG	AGACATTGGAGTGAACGCATCG
	β-catenin	ATAGAGGCTCTTGTGCGTACTGTC	TTGGTGTCGGCTGGTCAGATG
	cyclin D1	CGCCCTCGGTGTCCTACTTC	GACCTCCTCCTCGCACTTCTG
	GAPDH	TGACATCAAGAAGGTGGTGAAGCAG	GTGTCGCTGTTGAAGTCAGAGGAG
Danio rerio	*mtor*	ACTGCTGATGTGTCGTGATTTGG	AATGGACTGGATGCGTATGATTGAC
	lc3	CACAGTTATGCCATCCGACAGACC	GCTCTCGTATCTGCTGCACTTCC
	p62	CTAGGCTGGTGGAGTCTCTGTCTC	CTTGGTGTGGAGCAGTCTGGTTAG
	dna-pkcs	GGCTGCTGATACTTCCACTGTTG	ATTCGTGCTCACTGTGTCTTCAAG
	atm	GCCATCCTGTCCAAGACTCCAATG	CATCATCAGTATGCGGTGCCTCTC
	atr	GCAGGTGGACATGAAGAGCAGAAG	TGAACCGCACTCACGCATTGG
	chek1	AACCGCTTCACATGGGACAACG	ACCAGCAGTCGCACCTCTCC
	chek2	CAGGCGTCTGTGGTGAAGTGAAG	CGTGTGGCTGTCCCTATTGATGG
	p21	TCTCGTAGCAGCGTTATTGACAG	TCTCTGGAAGACTGAGGAATGGATC
	cdk2	CAGAATCTCCTCATCAACGCTCAG	TCCGCACAGGTACACCGAAC
	p15	TCTAACGGAGTGAATGCCAATGTG	CAGCAGCACAAGAGCCAAAGG
	β-catenin	CGGAGGATGACGATGTGGATAATC	CGATGTCTGCTACTTGCTCTTGG
	cyclin d1	GAGGAAAGGTTGATGGAGCAGGTC	GCTGTACTATACCGCAGGCTTACG
	gapdh	GACGCTGGTGCTGGTATTGC	CCATCAGGTCACATACACGGTTG

Statistics

Using GraphPad Prism 9.0 software (GraphPad Software, San Diego, CA, USA), statistical analysis was conducted. Each experiment was carried out independently at least three times ($n \geq 3$). Results are expressed as mean ± standard error (SEM). Group differences were analyzed with one-way analysis of variance (ANOVA). $p < 0.05$ was deemed statistically significant.

Results

Network pharmacology analysis

MT-targets network

33 active ingredients of MT and fourteen active compounds were identified in this study (Table 2) with OB ≥10 % and DL ≥0.18. After excluding targets with a prediction score of zero from SwissTargetPrediction, 851 targets were identified. The top ten targets of each active compound were retained to form the MT-target network (Fig. 2A).

Table 2

Effective active ingredients of MT.

Mol ID	Molecule name	OB (%)	DL
MOL002045	Stigmasterol	43.4	0.8
MOL002047	Melianone	40.7	0.8
MOL002054	Thujopsadiene	10.7	0.7
MOL002058	Medioresinol	57.2	0.6
MOL002043	Nimbolidin C	28.8	0.6
MOL002048	Nimbolidin D	30.4	0.5
MOL000515	Melissic acid	13.2	0.5
MOL000983	n-Triacontanol	10.5	0.5
MOL002044	Toosendanin	10.1	0.4
MOL002056	(E)-3-[(2S,3R)-2-(4-hydroxy-3-methoxy-phenyl)-7-methoxy-3-methylol-2,3-dihydrobenzofuran-5-yl] acrolein	54.7	0.4
MOL000098	Quercetin	46.4	0.3
MOL002053	Nimbolin A	32.1	0.3
MOL001495	Ethyl linolenate	46.1	0.2
MOL002056	Mandenol	42.0	0.2

The MT-core target network of liver toxicity

In the GeneCards database, 9632 related targets were obtained by entering the keyword “liver toxicity” and screened 871 targets with a relevance score >10. The active ingredients and liver toxicity targets were entered into the VENNY2.1.0 website, and 114 intersecting targets were identified (Fig. 2B). GO enrichment analysis of the 114 overlapping genes included cellular response to cadmium ions, cellular response to reactive oxygen species. KEGG pathways included the AMPK, p53, and mTOR signalling pathways (Fig. 2C). The 57 core targets of fourteen effective active ingredients form the MT active ingredient-core target network (Fig. 2D).

Molecular docking analysis of active compounds with target protein

The active compounds and ten core targets with the highest degree values were used for molecular docking, and the docking scores are presented as a heatmap (Fig. 2E). Negative docking scores, indicating unstable compound-target binding, were excluded. A heatmap of the docking scores of BCL2, HSP90AA1, MTOR, STAT3, SRC, AKT1, EGFR, and JUN with the thirteen compounds was retained. The total score was used to evaluate the binding affinity of the compounds to proteins. TO, a key bioactive marker component of MT, exhibited the highest docking score with mTOR (Fig. 2F). These findings suggested that mTOR is crucial for TO-induced liver toxicity.

Binding dynamics of the TO-mTOR complex

We further investigated the TO-mTOR complex using MD simulations. The RMSD curve indicated fluctuations in protein conformation. As shown in Fig. 3A and B, the RMSD values had a mean value of 4.4 Å, and the Rg values fluctuated within 1 Å. The average RMSF was 1.6 Å, and no amino acid residues showed conformational changes beyond 4 Å throughout the simulation. These results demonstrated the significant stability of the system (Fig. 3C). The phenylalanine (PHE) at position

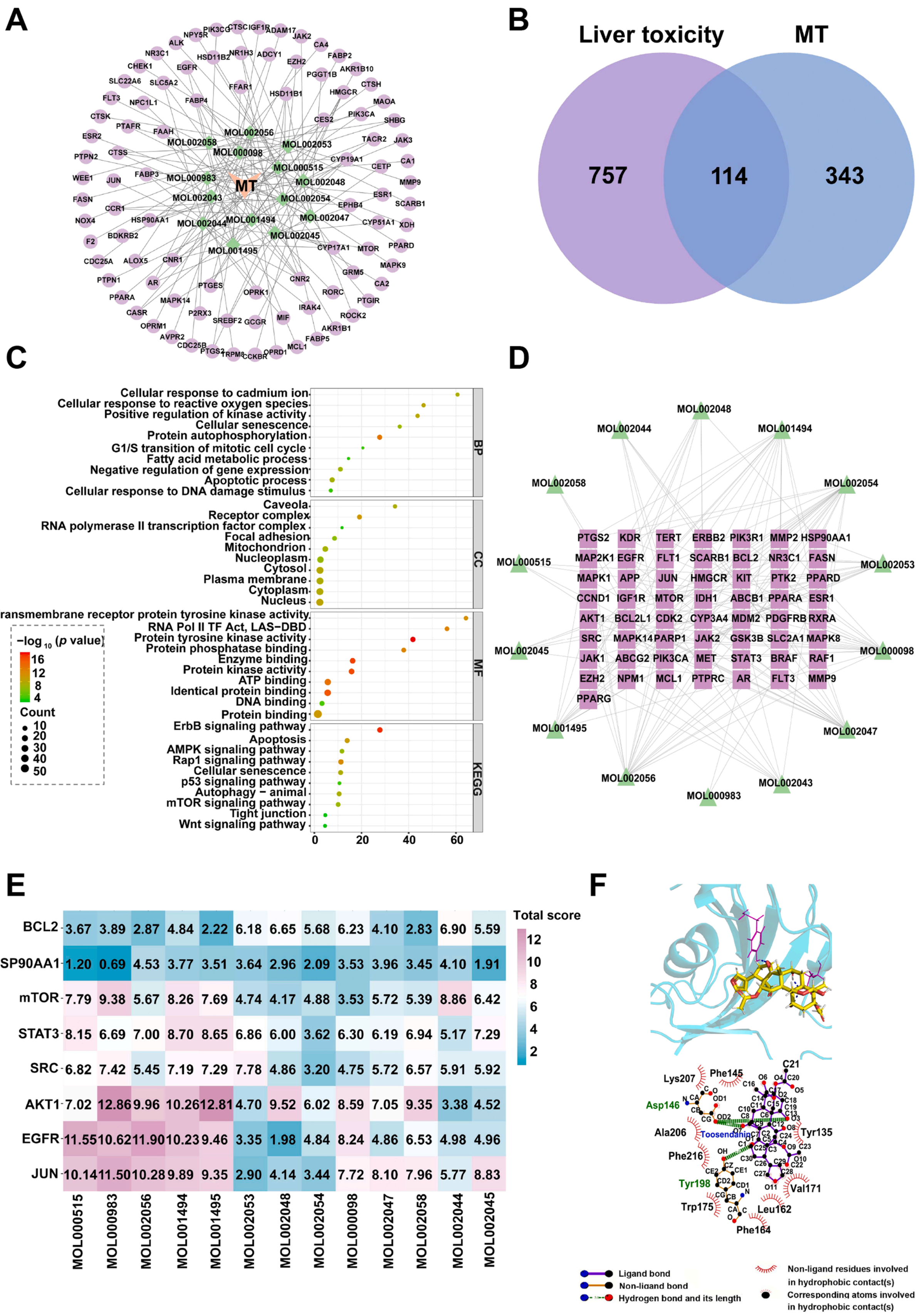

Fig. 2. TO network pharmacological results and validation. (A) MT-target network show the active ingredients of MT screened using TCMSP and predicted targets. (B) Venn diagram show the overlap of 114 targets genes of pharmacologically active compounds and liver toxicity relative genes. (C) GO and KEGG enrichment bubble plots. (D) PPI network diagrams of active ingredients and core targets of drugs. (E) Heatmap of the scores of key targets and active compounds of drugs. (F) Visualization of the docking results of the molecular interaction between TO and mTOR.

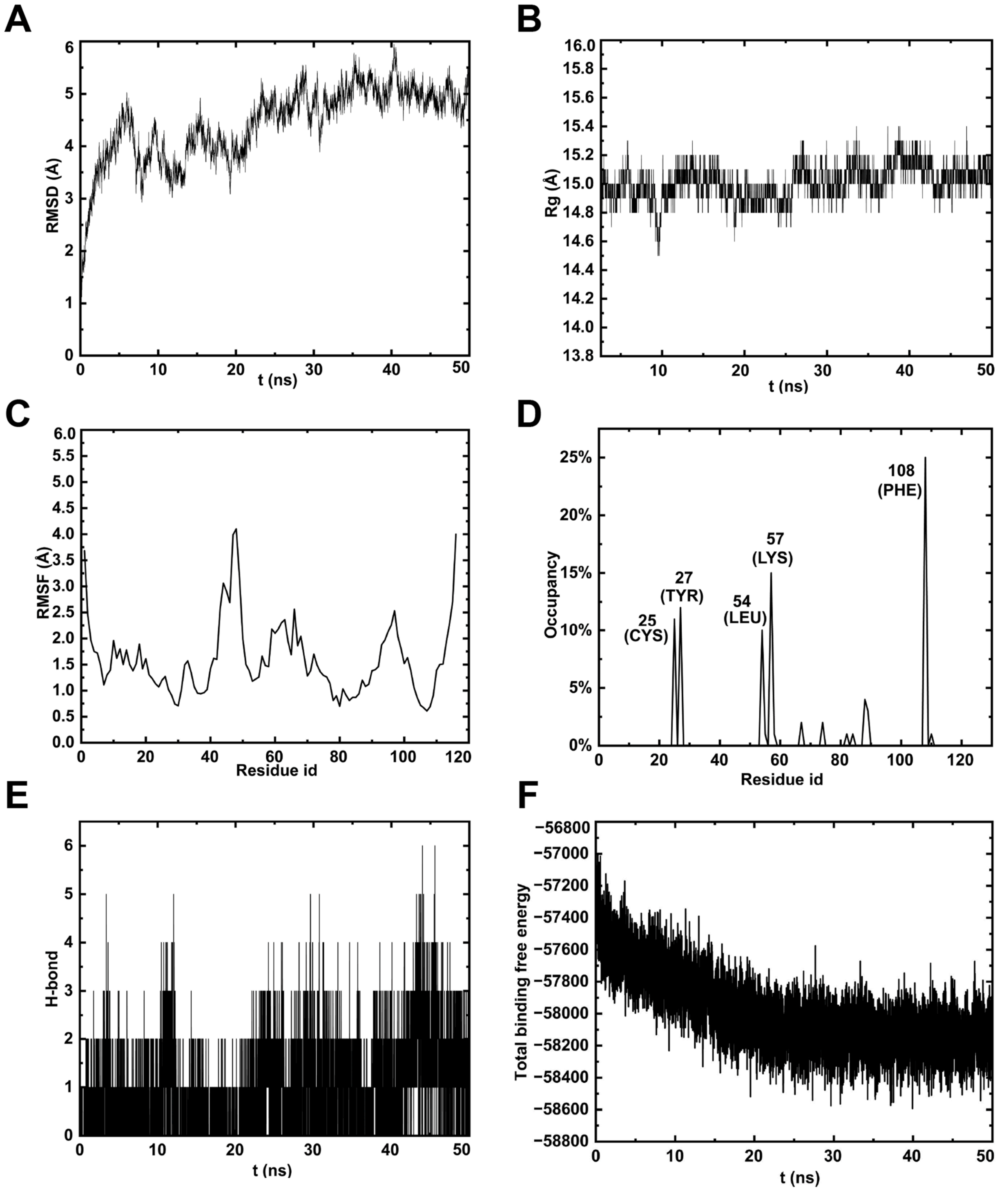

Fig. 3. MD simulation of TO-mTOR complex. (A) RMSD analyses demonstrated the stability of mTOR protein and its binding structures with TO. (B) The Rg of complex varies with time. (C) RMSF analyses indicate the binding stability of mTOR protein residues with TO. (D) H-bond occupancy of amino acids within the complexes. (E) Number of hydrogen bonds per ns. (F) Energy changes in the TO-mTOR complex over 50 ns during MD simulations.

108 displayed the maximum hydrogen bond occupancy of 25 % at 50 ns (Fig. 3D and E). The binding free energy of TO-mTOR complex steadily declined throughout the simulation, indicating that TO formed a stable bond with mTOR (Fig. 3F).

Impact of TO on autophagy

Network pharmacology and simulation analyses verified that TO may bind to mTOR and contribute to liver damage. Furthermore, subsequent high-throughput sequencing results exhibited a notable difference in p62 and LC3 after treatment, with *p* values of 5.83×10^{-195} and 2.09×10^{-76}, respectively, and $\log_2$(fold change) of 1.46 and 1.44 (Fig. 10C). Additionally, as shown in Fig. 4A–C, the reduction in p-mTOR and upregulation of LC3-II/LC3I indicated activated autophagy. However, the increased expression of p62 at both transcriptional and translational levels suggests that TO inhibits autophagy flow.

The cell viability and LDH leakage influenced by TO

The cytotoxicity of TO on HepG2 cells was assessed. Fig. 5A indicates

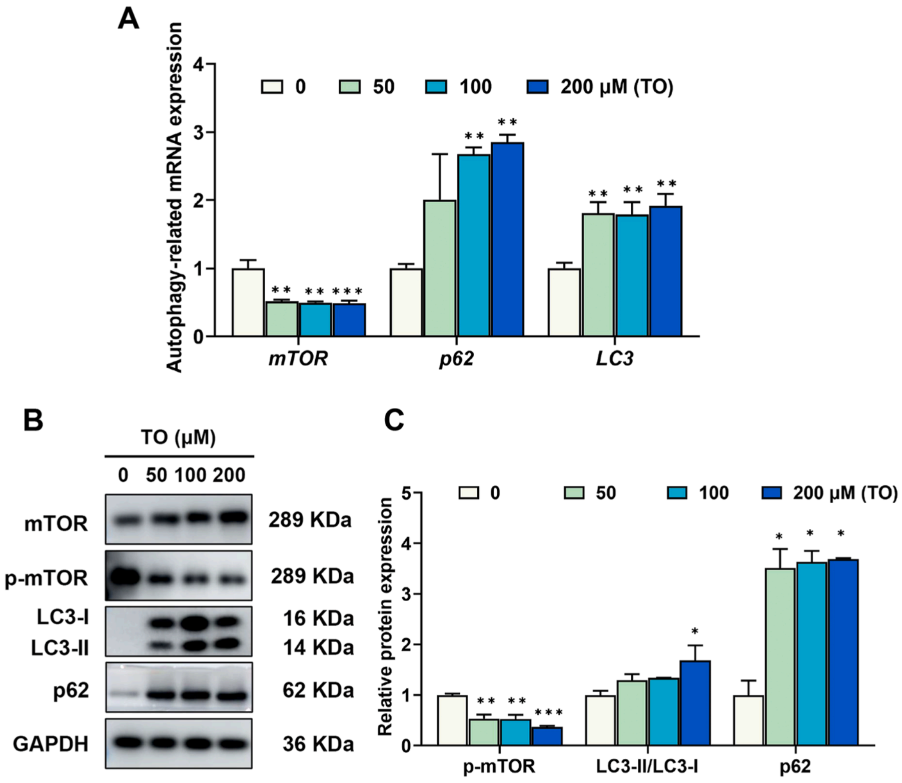

Fig. 4. Impact of TO on autophagy after 48 h in HepG2 cells. (A) The autophagy-related genes were analyzed using RT-qPCR. (B) Proteins involved in autophagy were evaluated using western blot analysis. (C) The gray values were quantified using ImageJ ($n = 3$), $*p < 0.05$, $**p < 0.01$, $***p < 0.001$.

that the reduction in cell viability following TO exposure is dose dependent. Specifically, at concentration of 50, 100, and 200 μM, the survival rate of HepG2 cells after 48 h were 81.4 %, 75.8 %, and 47.2 %, respectively. Additionally, the release of LDH in these three concentrations showed an increasing trend (Fig. 5B). These three concentrations were chosen for further experiments, with 100 μM as the sequencing concentration.

Transcriptome-wide analysis of m6A modifications

To investigate the mechanism of TO on liver injury, cells treated with 100 μM TO were selected for mRNA-seq and MeRIP-seq analysis. The principal component analysis (PCA) revealed TO treated group formed a distinct cluster from the untreated cells (Fig. 5C). Notably, 217 m6A-modified genes were unique to the TO-treated cells (Fig. 5D), where the R package exomePeak2 (Suzhou, China) (Meng et al., 2013; Wu et al., 2022) identified 34,943 m6A peaks across 7919 genes, compared to 43,674 in 9211 genes in the control group (Fig. 5E). The m6A consensus motif for RRACH showed the classical motif in both CON and TO groups (Fig. 5F). Furthermore, most genes exhibited fewer than three or more than eight m6A methylation peaks (Fig. 5G), with the distribution of m6A methylation mainly located within the coding sequences (CDS) as depicted in Fig. 5H. Among these, 44 % of the m6A-modified genes and 12 % of the m6A peaks were associated with disease (Fig. 5I).

Differentially methylated genes

Using the criteria of $p < 0.05$ and $|\log_2(\text{fold change})| > 0.263$, 1488 overlapping genes between 5472 differentially expressed genes and 3955 differentially m6A-modified genes (Fig. 6A) were identified. Among these, 780 genes were activated, and 708 were suppressed (Fig. 6B). The KEGG and GO enrichment analysis of the mentioned overlapping genes, conducted using the DAVID database, revealed associations with lysosome, cellular senescence, DNA replication, MAPK signaling pathway, and cell cycle (Fig. 6C). The GO enrichment analysis corresponded to cellular responses to DNA damage stimulus (biological process, BP), mitochondrion (cell component, CC), and protein binding (molecular function, MF), etc. (Fig. 6D). As shown in heat map (Fig. 6E), TO treatment resulted in either significantly lower or higher gene expression levels in the KEGG pathways. To explore the specific trends, the gene set enrichment analysis (GSEA) analysis revealed a downward trend in DNA replication and cell cycle pathways, while the lysosome pathway which indicated the autophagy exhibited an upward trend (Fig. 6F–H).

Regulatory analysis of RNA m6A methylation following TO treatment

The expression of m6A demethylases (erasers), recognition proteins (readers), and methyltransferases (writers) were assessed following 48 h treatment with 100 μM TO. The significant down-regulation of the readers *HNRNPC, HNRNPA2B1*, and *FMR1,* as well as the writers *VIRMA, ZC3H13, METTL3, METTL5*, and *RBM15B1* ($p < 0.05$) was observed, with *HNRNPC* exhibiting the most pronounced decrease (Fig. 7A, B). This suggests that TO may reduce the level of m6A methylation.

Using CLIP-seq datasets, further investigation was conducted on the potential substrates of these regulators. As show in Fig. 7C–F, HNRNPC significantly regulates most genes involved in cell cycle, DNA replication, cellular senescence, and lysosome. Regulatory relationships among these genes are illustrated in a PPI network analysis using STRING (Fig. 7G). Additionally, m6A methylation of cell cycle genes, including cyclin-dependent kinase 2 (*CDK2*) and *p15*, was found to be reduced (Fig. 7H).

TO induced oxidative stress and calcium overload in HepG2 cells

ROS refers to a group of highly reactive molecules (Cheung and Vousden, 2022), that are more likely to cause DNA damage (Kong and Chandel, 2018; Winterbourn, 2020). As shown in Fig. 8A, 100 μM TO treatment showed increased ROS accumulation in comparison to the control, and the effect was exacerbated with 200 μM TO ($p < 0.01$). Furthermore, MDA level was increased(Fig. 8B), with decreased

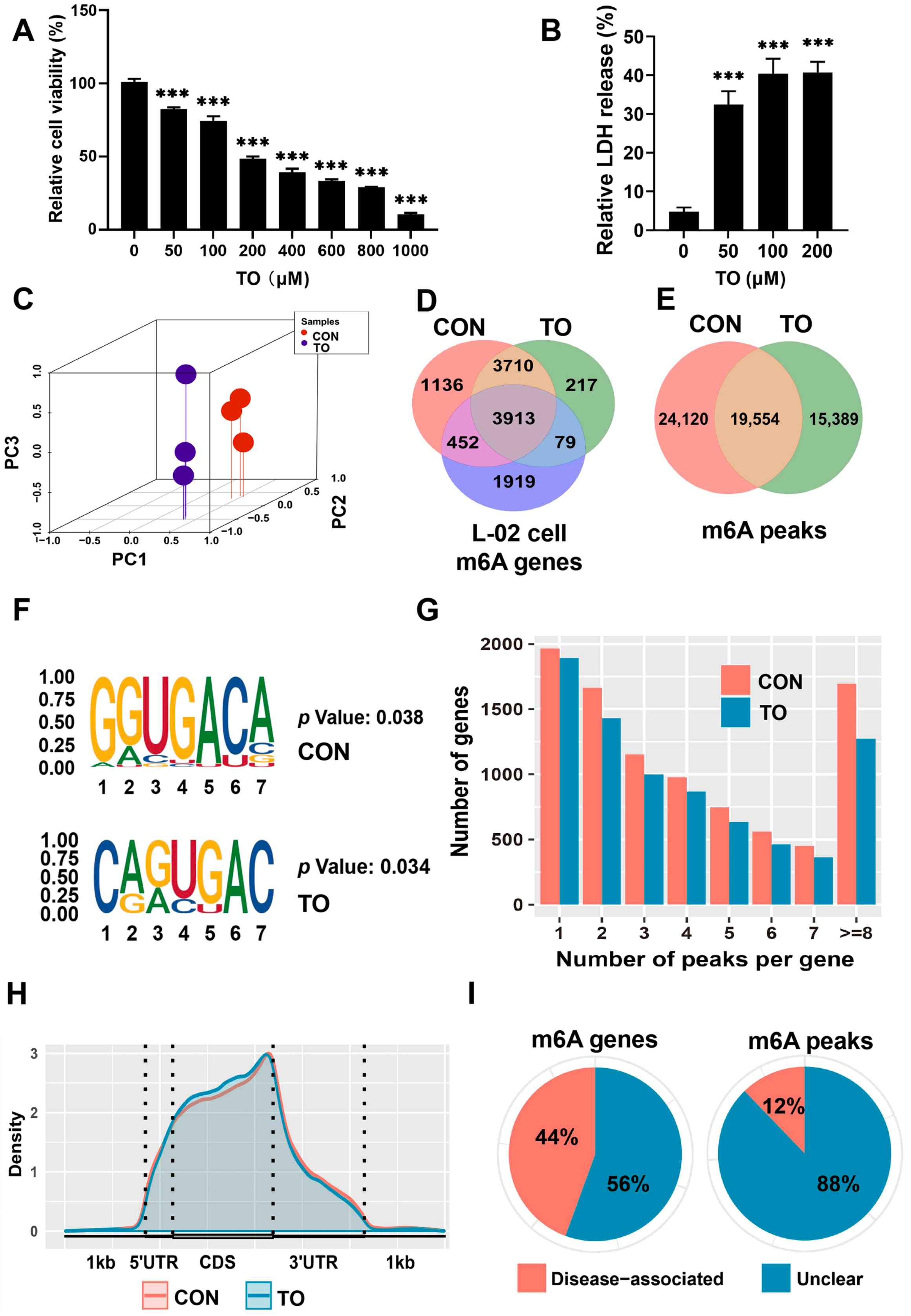

Fig. 5. Transcriptome-wide analysis of m6A modifications following 48 h TO exposure in HepG2 cells. (A) MTT assay results demonstrate the relative cell viability following 48 h of TO treatment. (B) Cell LDH leakage levels after TO treatment for 48 h, $n = 3$, $***p < 0.001$. (C) PCA analysis was conducted to demonstrate differentiation between the CON and TO groups. (D) The overlap of m6A genes among CON, TO and L-02 cell groups. (E) The m6A peaks in CON and TO groups. (F) The m6A consensus motif for RRACH. (G) The number of m6A methylation peaks, and (H) the m6A modification peaks' density within mRNA transcripts. (I) The effect of m6A peaks and m6A genes on disease after treatment with TO.

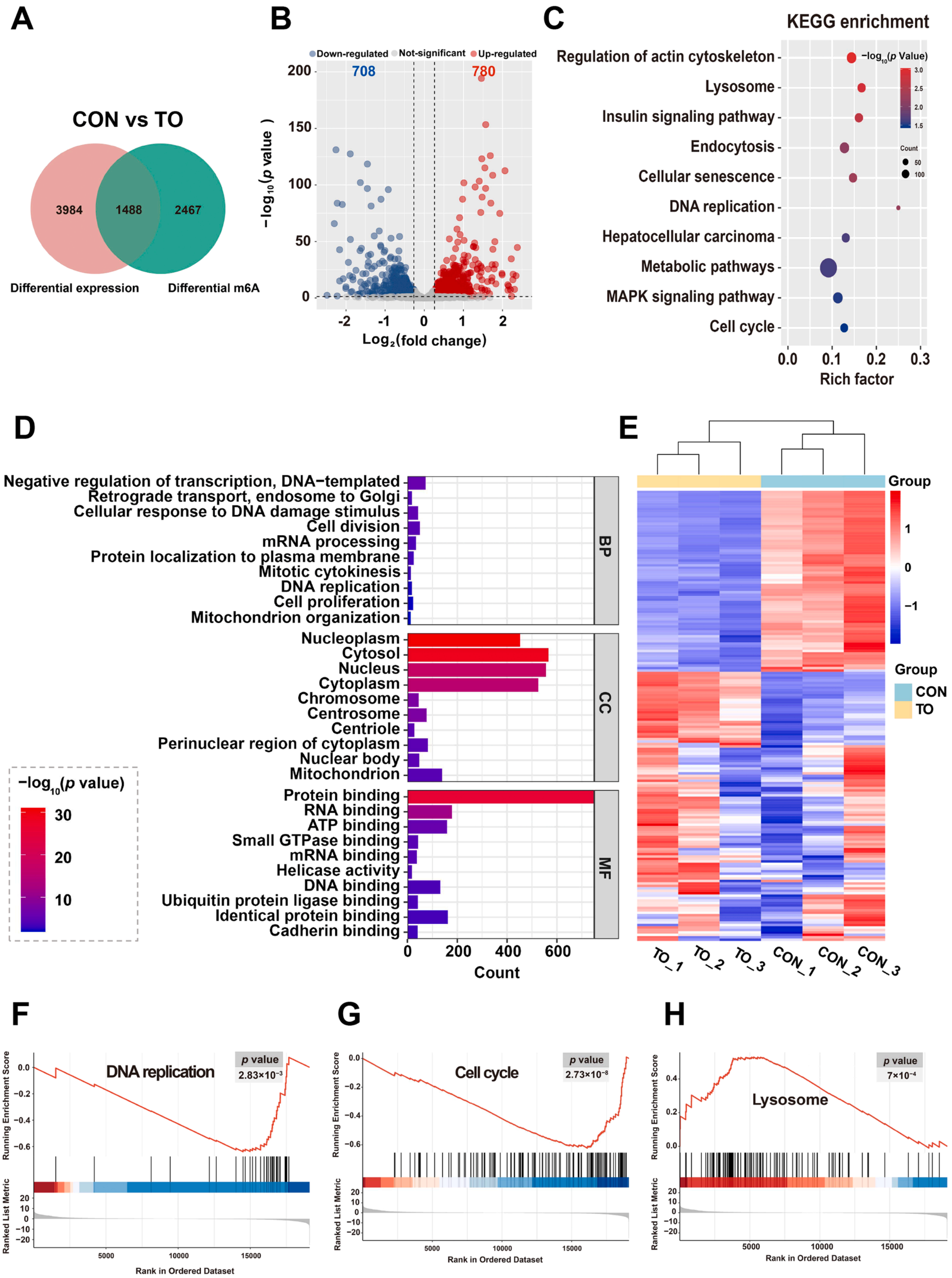

Fig. 6. Differentially methylated genes following 48 h TO exposure in HepG2 cells. (A) A total of 1488 overlapping differentially methylated genes were found with $p < 0.05$ and $|\log_2(\text{fold change})| > 0.263$. (B) Volcano plot analysis, (C) KEGG enrichment, and (D) GO enrichment were performed on the differentially methylated genes between the CON and TO groups. (E) The heat map shows the differentially methylated genes related to DNA replication, cell cycle, lysosome, cellular senescence, and metabolic pathway in the CON and TO groups. GSEA analysis highlights specific trends in (F) DNA replication, (G) cell cycle, and (H) lysosome following TO treatment.

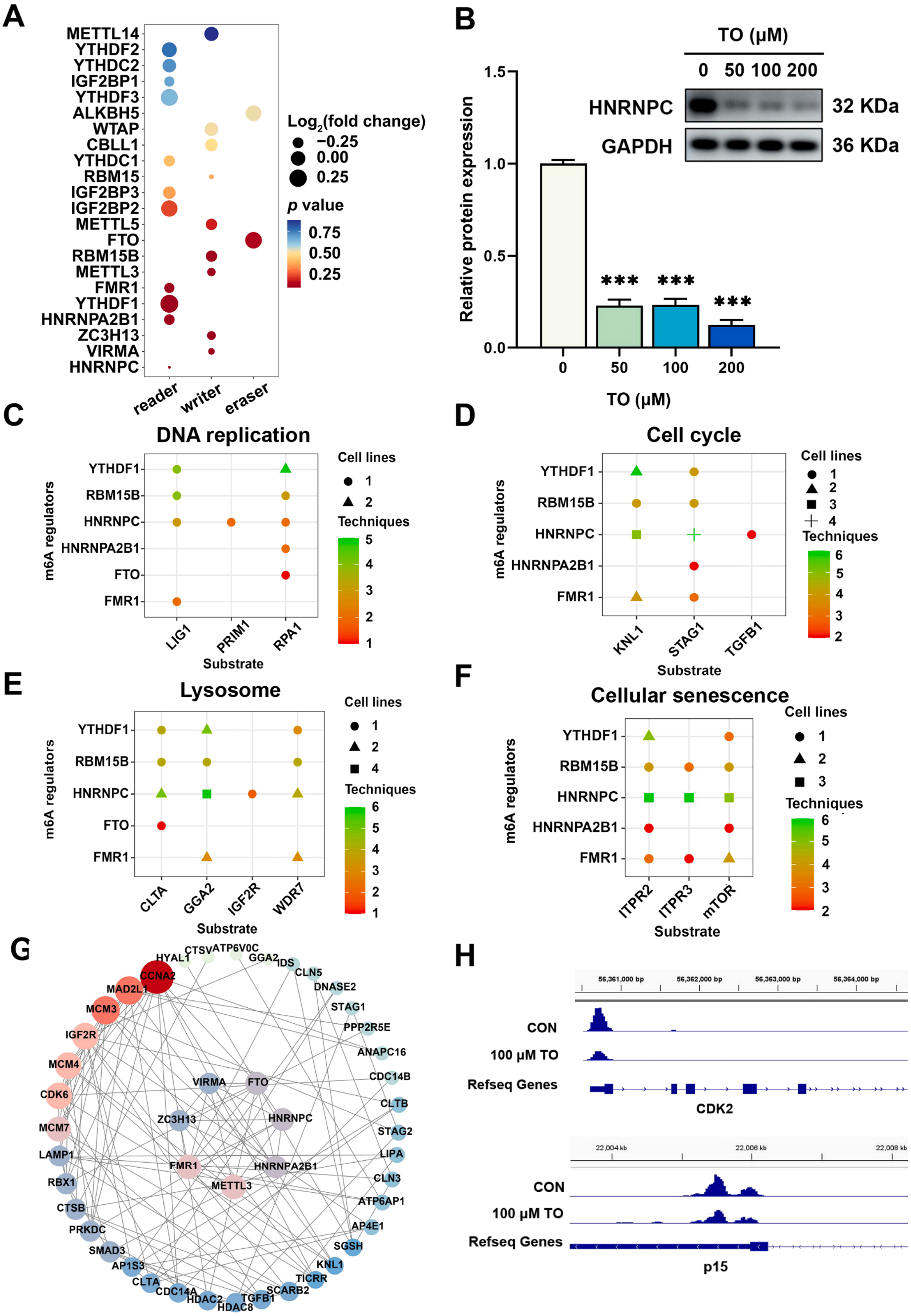

Fig. 7. Regulatory analysis of RNA m6A methylation following 48 h TO exposure in HepG2 cells. (A) The p value and $\log_2$(fold change) of m6A regulators are presented, along with (B) western blot analysis of HNRNPC. Potential substrates of these regulators including genes related to (C) DNA replication, (D) cell cycle, (E) lysosome, and (F) cellular senescence. (G) A PPI network illustrates the regulatory relationships among these genes. (H) IGV analysis demonstrates a reduction in m6A methylation in CDK2 and p15 ($n = 3$), $***p < 0.001$.

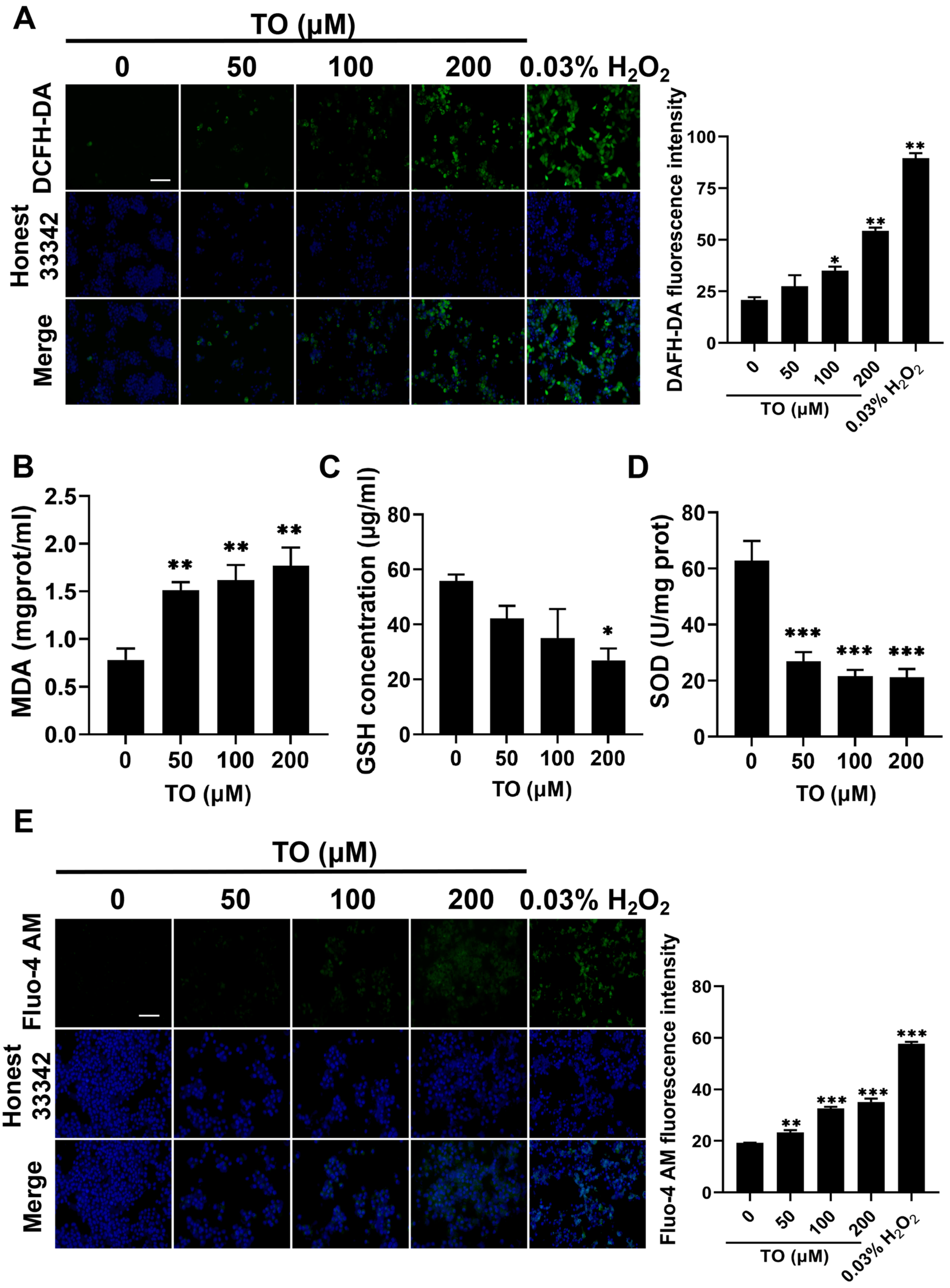

Fig. 8. Oxidative stress and calcium overload after 48 h TO exposure in HepG2 cells. (A) Fluorescence images and quantitative results of ROS detected using DCFH-DA probe. Intracellular (B) MDA, (C) GSH, (D) SOD detected using assay kits. (E) Fluorescence images and quantitative results of Ca^{2+} detected using Fluo-4 AM. $n = 3$, $*p < 0.05$, $**p < 0.01$, $***p < 0.001$.

antioxidant factors, such as GSH and SOD (Fig. 8C and D). These indicate TO induces oxidative stress in HepG2 cells. In Fig. 8E, fluo-4 AM levels were quantified as 19.21 ± 0.12, 23.32 ± 0.81, 32.54 ± 0.72, and 35.12 ± 1.32 in 0, 50, 100, and 200 μM TO treatments, respectively. It indicated that TO treatment led to high levels of calcium accumulation.

TO induced mitochondrial damage

mRNA-seq analysis revealed that TO impacted mitochondrial function, which was assessed *via* mPTP, MMP, and mitochondrial activity. Calcein fluorescence intensity were 95.01 ± 1.16, 60.14 ± 2.63, 42.86 ± 1.43, and 35.33 ± 0.89 in the 0, 50, 100, and 200 μM TO treatment, which means increased mPTP opening in HepG2 cells (Fig. 9A). At the same time, the ratio of JC-10 multimer to monomer in each treatment group decreased with the increase of TO dose, showing a significant dose-dependent effect (Fig. 9B). Consistent with these findings, the quantification of mito-tracker red CMXRos was weakened after TO treatment ($p < 0.001$), suggesting that mitochondrial activity of HepG2 cells was impaired after TO treatment (Fig. 9C).

Impact of TO on DDRs

Hoechst 33342 could attache to double-stranded DNA, emitting blue fluorescence when excited using blue light. As show in Fig. 10A, nuclear fragments indicating DNA damage are evident following TO treatment. In response to DSBs, γ-H2AX rapidly accumulates at the damage sites, which is essential for restructuring chromatin and facilitating the recruitment of factors involved for DNA repair (Song et al., 2024). In Fig. 10B, the fluorescence intensities of γ-H2AX increased, with values of 79.34 ± 2.93 and 96.36 ± 3.39 for the 100 μM and 200 μM groups, respectively. However, the expression of DNA-PKcs, ATM, ATR, checkpoint kinase 2 (CHEK2), p53, and p21 showed significant reductions at both the mRNA, as identified using mRNA-seq and RT-qPCR, and western blot (Fig. 10C–E). These indicating a repression of the DDRs which may hinder the repair of mutated genes.

TO induces G1/S phase arrest in HeG2 cells

To ensure the repair of substantial DNA damage, cell cycle checkpoints and DNA repair pathways has evolved. As shown in Fig. 11A, treatment with 100 μM TO leaded to an obvious increase in S phase, rising from 22.2 ± 1.19 % to 39.5 ± 2.34 % (Fig. 11B). This indicates TO effectively triggered arrest of cell cycle at G1/S phase. The expression of G1/S phase-related protein CDK2, along with G1 phase-related proteins cyclin E1, p15, β-catenin, and cyclin D1, were acessed using qPCR and western blot analysis (Fig. 11C–E). The findings revealed a reduction in the protein levels of CDK2, cyclin E1, β-catenin, and cyclin D1, while there was a significant increase in the expression of p15. It follows that TO inhibited the proliferation of HepG2 cells and causes to arrest in the G1/S phase.

Hepatotoxicity induced by TO in vivo

Zebrafish larvae were used to clarify the *in vivo* toxic effects of TO. Fig. 12A and B reveal a significant rise in malformation rate alongside a reduction in survival rate. The surviving zebrafish larvae showed a significantly decreased body length (Fig. 12C). Behavioral tests were conducted after TO treatment to investigate the abnormal behavioral change, including movement distance, velocity, and duration (Fig. 12D–G). As show in the Fig. 12H and I, TO-treated groups showed a significant reduction in liver area and GSH, and increased ROS, AST, and ALT levels (Fig. 12I–M). In addition, TO changed the expression of genes associated with DDRs, cell cycle, and autophagy, including a decrease in *mtor, dna-pkcs, atm, atr,* checkpoint kinase 1 (*chek1), chek2, p21, cdk2, β-catenin,* and *cyclin d1,* while an increase in the autophagy-related genes *p62, lc3, and p15* (Fig. 12N).

Discussion

MT is commonly used as an insecticide for the treatment of gastrointestinal parasites. However, it has been documented it can cause severe liver injury, which limits its application (Zheng et al., 2015). Network pharmacological analyses revealed that TO, thujopsadiene, acrolein, quercetin, mandenol, and melianone are the main compounds responsible for liver toxicity. This study focuses on TO, a key bioactive marker compound in MT present at concentrations between 0.04 % and 0.20 % (Chinese Pharmacopoeia Committee, 2020), and its role in MT-induced liver toxicity. It is the first to comprehensively link impact of TO on oxidative stress, DDRs inhibition, cell cycle arrest, and autophagy flow disruption (Fig. 13).

Network pharmacology analysis showed that cellular response to ROS was significantly enriched, which could trigger mitochondrial damage (van Hameren et al., 2019; Zorov et al., 2014). HepG2 cells treated with TO exhibited this imbalance along with a simultaneous mitochondrial permeability transition. This suggests that TO damages cells by elevating ROS levels, which leads to Ca^{2+} overload and mitochondrial dysfunction. Such damage can act as a catalyst for autophagy activation, leading to function in eliminating dysfunctional components. In the present study, mTOR was enriched in network pharmacological analysis and exhibited the highest docking score with TO. Inactivation of mTOR disrupts autophagy inhibition (Ganley et al., 2009), leading to significant upregulation of LC3-II/LC3-I. However, the accumulation of p62, a marker of autophagic flux, results from defective autophagy (Kumar et al., 2022). This suggests that activated autophagy is disrupted after TO treatment, which lead to excessive damage and hepatocyte death (Allaire et al., 2019; Ke, 2019).

To examine the molecular processes underlying TO-induced hepatocyte injury, the mRNA transcriptional profiles and RNA m6A epigenetic alterations were analyzed. Notably, 44 % of m6A-modified genes induced by TO were associated with disease. Consequently, 1488 differentially expressed genes with m6A modifications were screened and performed KEGG and GO enrichment analyses. These analyses revealed significant enrichment in cell cycle, DNA replication, and lysosome pathways. To further understand the molecular effects of m6A modifications, the roles of readers and writers (Zhao et al., 2020) were investigated, and these were found to be significantly downregulated following treatment. It suggested that the reduced m6A modification induced by TO may destabilise the mRNA of genes involved in cell cycle, DNA replication, and lysosome (König et al., 2010; Fan et al., 2021).

Differentially methylated gene enrichment analysis revealed the downregulation of cell cycle and DNA replication pathways. The fragmented remnants of HepG2 cell nuclei and accumulation of γ-H2AX further confirmed DNA damage following treatment, potentially caused by increased levels of ROS (Yahata et al., 2011). For repair, DNA-PKcs functions as an active protein kinase, forming an association with Artemis, the only vertebrate nuclease capable of opening DNA hairpins. This interaction enhances the nuclease activity of Artemis (Chang and Lieber, 2016). The repression of DNA-PKcs suppresses ATM and ATR at the transcriptional level (Chang and Lieber, 2016), resulting in the inactivation of CHEK1 and CHEK2, which in turn affects the activation of p53 (Lanz et al., 2019). Tumour suppressor protein p53 has been shown to target p21 to arrest the cell cycle (Smith et al., 1994). Inhibition of these proteins may lead to failure of DNA repair, and the accumulation of mutations or chromosome loss.

The retaining the effect of cell cycle arrest may be linked to changes in cyclin protein accumulation dynamics. In eukaryotic cells, cell cycle regulation is primarily governed by CDK activity. CDK2 is activated by cyclin E binding and is essential for facilitating DNA synthesis from the late G1 phase to S phase (Dietrich et al., 2024; Hu et al., 2014). Reduced CDK activity can lead to genomic instability, potentially resulting in cell death. Additionally, TO activates p15, a tumour suppressor gene typically silenced by methylation, and encoded by CDKN2B genes. p15 competes with cyclin D1 for binding to CDK4 and CDK6, inhibiting the phosphorylation of Rb products, thereby blocking progression through the G1/S phase (Otsuji et al., 2024). Furthermore, β-catenin, which, upon accumulation and translocation to the nucleus, activates cell proliferation genes (Yang et al., 2024). Low β-catenin levels may influence cyclin D1 transcription. Overall, TO influences cell cycle progression through intricate interactions involving cyclin proteins and tumour suppressor genes, resulting in G1/S phase arrest.

Conclusion

Collectively, our study offers a comprehensive analysis of TO in hepatotoxicity induction. TO reduced ATM and ATR levels by repressing DNA-PKcs, leading to irreparable damage and cell cycle disruption, particularly blocking the G1/S phase. Additionally, autophagy

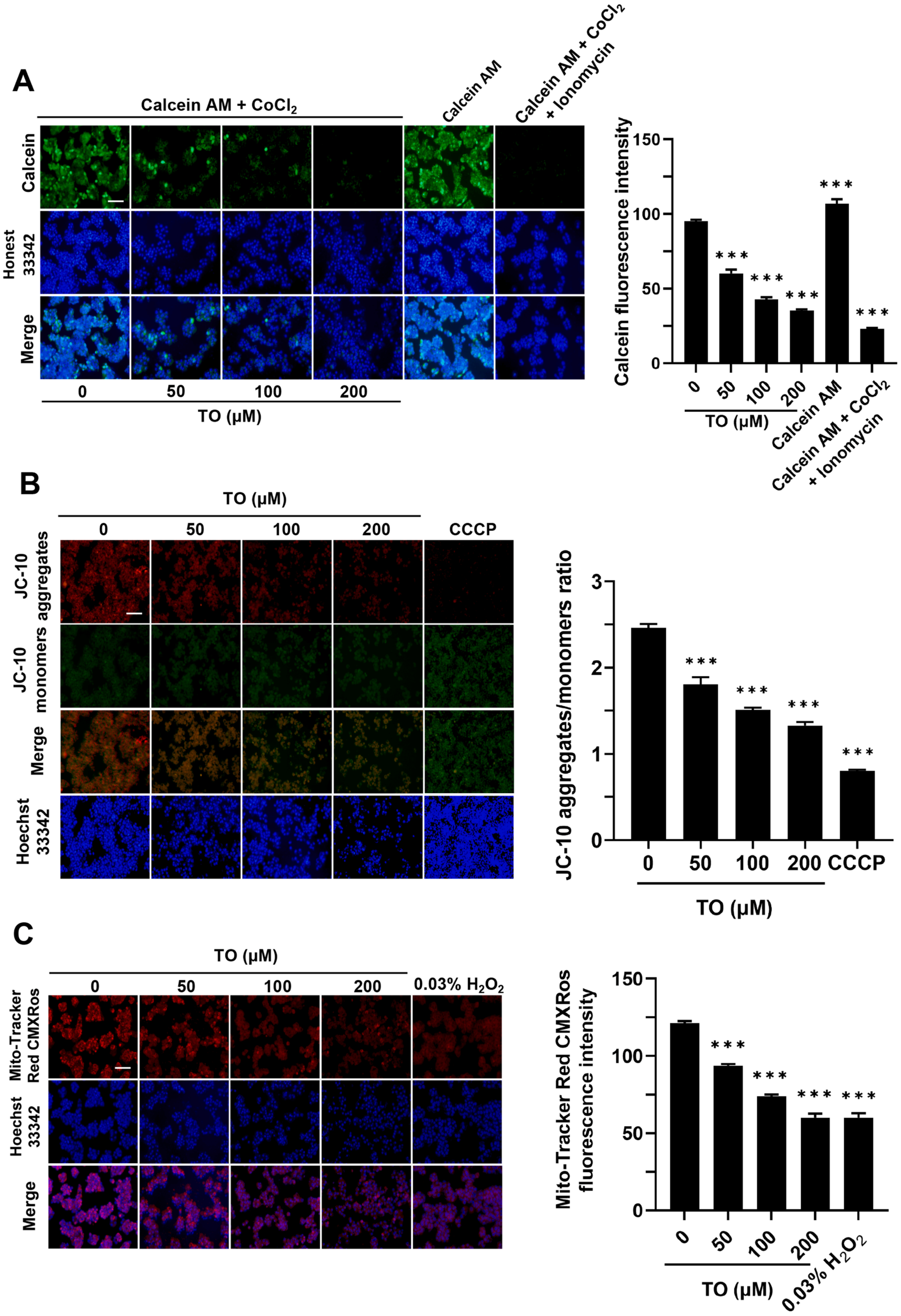

Fig. 9. TO induced mitochondrial damage after 48 h TO exposure in HepG2 cells. (A) Fluorescence images and quantitative results of (A) mPTP and (B) MMP detected using JC-10 probe. (C) Fluorescence images and quantitative results of mitochondrial activity detected using mito-tracker red CMXRos probe. Data are expressed as mean ± SEM for each group, $n = 3$, ***$p < 0.001$, scale bar =5 μm.

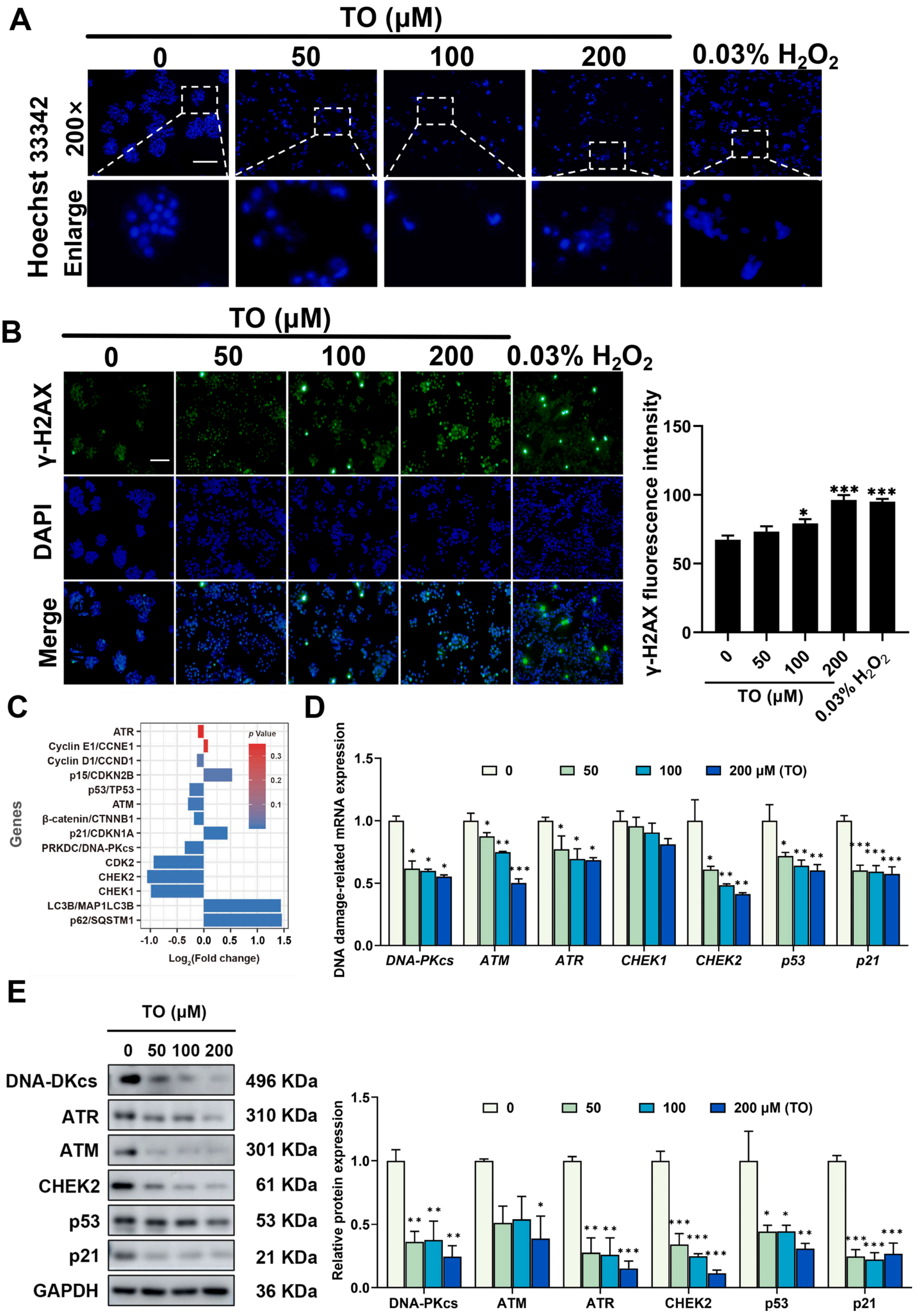

Fig. 10. Impact of TO on DDRs in HepG2 cells following 48 h exposure. (A) Hoechst 33342 staining was performed to visualize nuclear fragments. (B) Fluorescence images and intensity of γ-H2AX. Relative mRNA expression level was assessed using (C) mRNA-seq and (D) RT-qPCR. (E) Relative proteins expression and the gray values quantified using ImageJ. Data are presented as mean ± SEM for each group, $n = 3$, *$p < 0.05$, **$p < 0.01$, and ***$p < 0.001$, scale bar =5 μm.

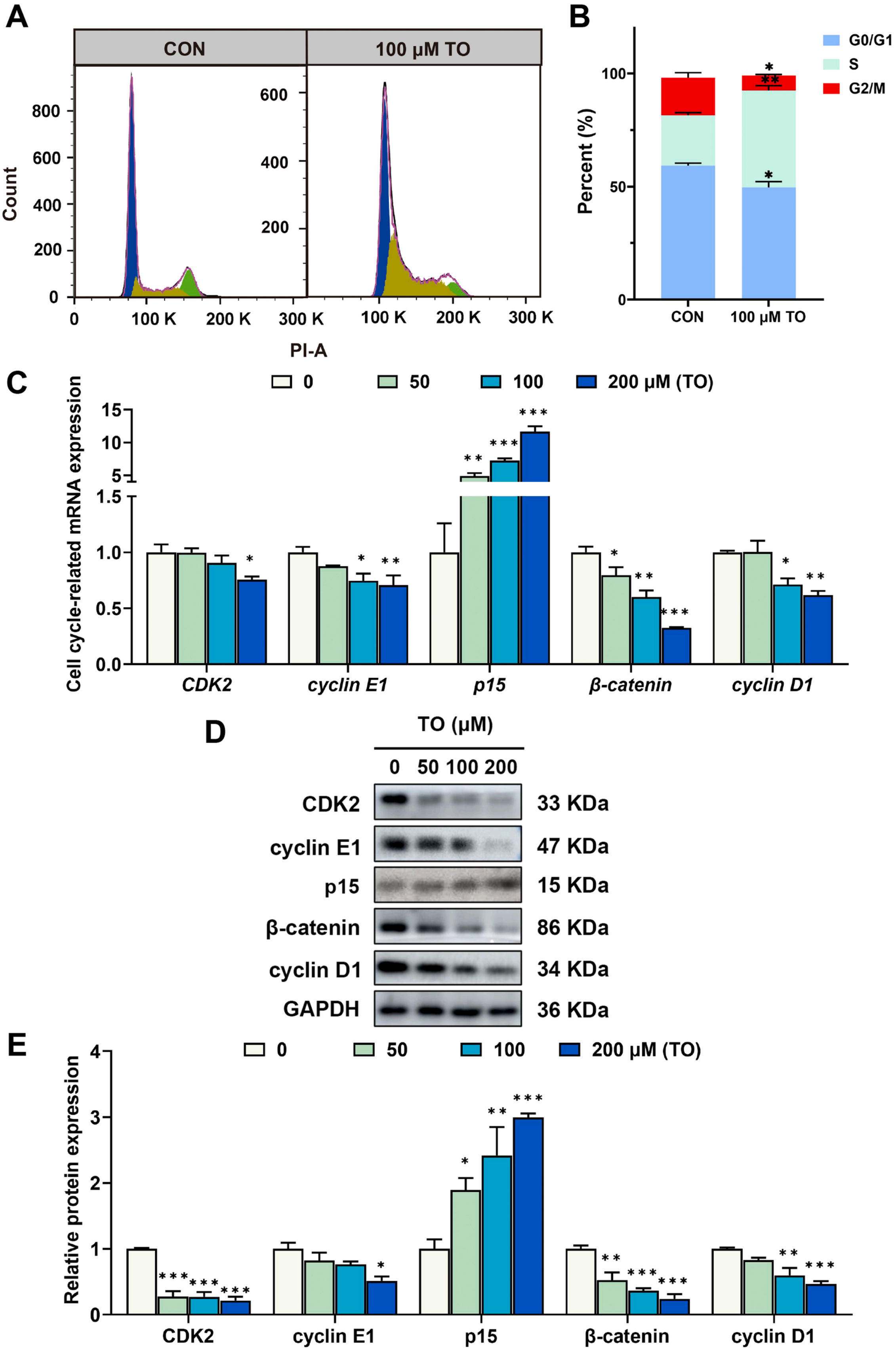

Fig. 11. TO induces G1/S phase arrest in HepG2 cells after 48 h treatment. (A) Cell cycle progression was detected using flow cytometry, and (B) calculated using Flowjo and ImageJ. (C) The mRNA level of cell cycle-relative genes in HepG2 cells were detected using RT-qPCR. (D) The protein levels were evaluated using western blot analysis, and (E) the blot density was quantified with ImageJ. Data are expressed as mean ± SEM for each group, $n = 3$, $*p < 0.05$, $**p < 0.01$, and $***p < 0.001$.

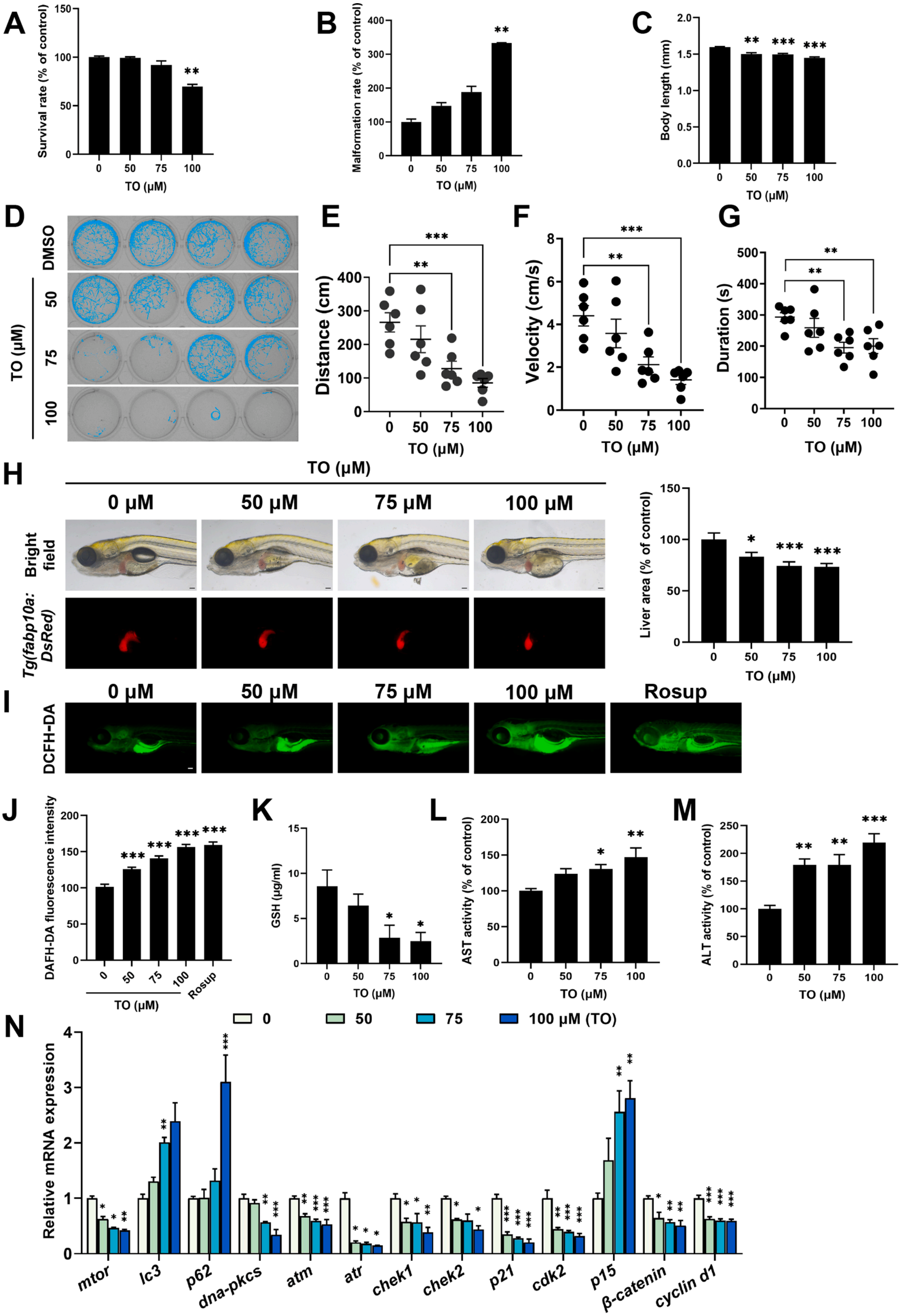

Fig. 12. Hepatotoxicity induced by TO following 72 h *in vivo.* (A) Survival rate, (B) malformation rate of zebrafish larvae. (C) Body length of zebrafish larvae, $n = 15$. (D) The locomotor behavior of zebrafish larvae was assessed. Statistical findings for (E) locomotor distance, (F) velocity, and (G) movement duration, $n = 6$. (H) Fluorescence images and quantitative results of zebrafish larvae liver, $n = 13$. (I) Fluorescence images and (J) quantitative results of ROS level, $n = 15$. (K) GSH, (L) AST and (M) ALT levels after 72 h. (N) Relative genes expression in zebrafish larvae, $n = 3$. Data are expressed as mean ± SEM for each group $^{*}p < 0.05$, $^{**}p < 0.01$, $^{***}p < 0.001$, scale bar =5 μm.

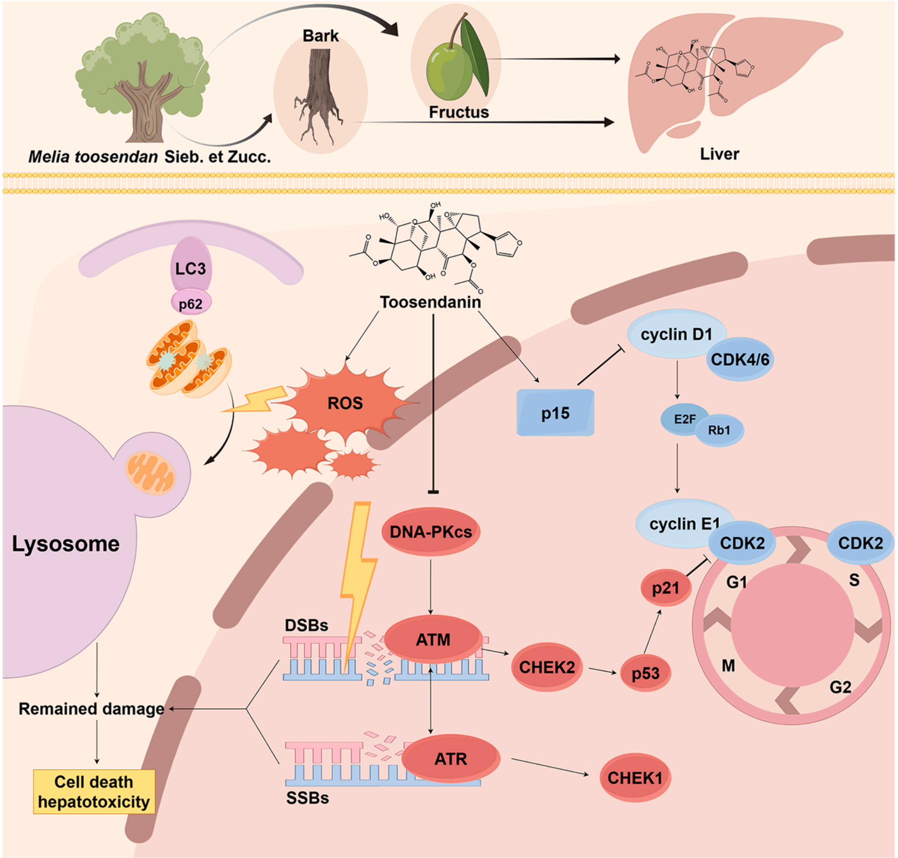

Fig. 13. Illustration of the signaling pathway related to the molecular mechanisms of TO toxicity.

dysfunction exacerbates cellular component damage, further contributing to hepatotoxicity.

Data availability statement

The data underlying the original contributions of this study can be accessed publicly at the GEO database, with the accession number GSE275885.

CRediT authorship contribution statement

Yifan Lin: Writing – original draft, Software, Methodology, Data curation. **Jian Zhang:** Writing – original draft, Investigation. **Xinyue Gao:** Writing – original draft, Investigation. **Zekai Wu:** Methodology, Funding acquisition, Data curation. **Lele Yang:** Formal analysis, Data curation. **Kun Tian:** Formal analysis, Data curation. **Xiaoqi Lv:** Methodology, Formal analysis, Data curation. **Jiaqi Li:** Writing – original draft, Investigation. **Kunqi Chen:** Methodology, Formal analysis, Data curation. **Youbo Zhang:** Methodology, Funding acquisition, Formal analysis. **Hong Hu:** Writing – original draft. **An Zhu:** Writing – review & editing, Project administration, Investigation, Funding acquisition, Data curation, Conceptualization.

Declaration of competing interest

The authors declare that they have no known competing financial interests or personal relationships that could have appeared to influence the work reported in this paper.

Acknowledgments

We wish to thank the financial support from the National Natural Science Foundation of China (82104520), the Fujian Medical University High-level Talent Research Startup Funding Project (XRCZX2023003), the Open Research Fund of Fujian Key Laboratory of Tumor Microbiology (FMUTM-202301). We appreciate the Public Technology Service Center, Fujian Medical University for providing the experimental platform and technical guidance for flow cytometry. The graphic abstract was drawn at https://www.figdraw.com/static/index.html#/.

References

Allaire, M., Rautou, P.E., Codogno, P., Lotersztajn, S., 2019. Autophagy in liver diseases: time for translation? J. Hepatol. 70, 985–998.

Atanasov, A.G., Zotchev, S.B., Dirsch, V.M., Supuran, C.T., 2021. Natural products in drug discovery: advances and opportunities. Nat. Rev. Drug Discov. 20, 200–216.

Chang, H.H., Lieber, M.R., 2016. Structure-specific nuclease activities of Artemis and the Artemis: DNA-PKcs complex. Nucleic Acids Res. 44, 4991–4997.

Cheung, E.C., Vousden, K.H., 2022. The role of ROS in tumour development and progression. Nat. Rev. Cancer 22, 280–297.

Chinese Pharmacopoeia Committee, 2020. Chinese Pharmacopoeia. China Medical Science Press, p. 44, 1.

Dietrich, C., Trub, A., Ahn, A., Taylor, M., Ambani, K., Chan, K.T., Lu, K.H., Mahendra, C. A., Blyth, C., Coulson, R., Ramm, S., Watt, A.C., Matsa, S.K., Bisi, J., Strum, J., Roberts, P., Goel, S., 2024. INX-315, a selective CDK2 inhibitor, induces cell cycle arrest and senescence in solid tumors. Cancer Discov. 14, 446–467.

Fan, J., Li, H., Xie, R., Zhang, X., Nie, X., Shi, X., Zhan, J., Yin, Z., Zhao, Y., Dai, B., Yuan, S., Wen, Z., Chen, C., Wang, D.W., 2021. LncRNA ZNF593-AS alleviates contractile dysfunction in dilated cardiomyopathy. Circ. Res. 128, 1708–1723.

Fan, W., Fan, L., Wang, Z., Yang, L., 2021. Limonoids from the genus *melia* (Meliaceae): phytochemistry, synthesis, bioactivities, pharmacokinetics, and toxicology. Front. Pharmacol. 12, 795565.

Fu, H., Zhu, X., Di, Q., Sun, J., Jiang, Q., Xu, Q., 2023. m6A contributes to a pro-survival state in GC-2 cells by facilitating DNA damage repair: novel perspectives on the mechanism underlying DEHP genotoxicity in male germ cells. Sci. Total. Environ. 859, 160432.

Howe, K., Clark, M.D., Torroja, C.F., Torrance, J., Berthelot, C., Muffato, M., Collins, J.E., Humphray, S., McLaren, K., Matthews, L., McLaren, S., Sealy, I., Caccamo, M., Churcher, C., Scott, C., Barrett, J.C., Koch, R., Rauch, G.J., White, S., Chow, W., Kilian, B., Quintais, L.T., Guerra-Assunção, J.A., Zhou, Y., Gu, Y., Yen, J., Vogel, J.H., Eyre, T., Redmond, S., Banerjee, R., Chi, J., Fu, B., Langley, E., Maguire, S.F., Laird, G.K., Lloyd, D., Kenyon, E., Donaldson, S., Sehra, H., Almeida-King, J., Loveland, J., Trevanion, S., Jones, M., Quail, M., Willey, D., Hunt, A., Burton, J., Sims, S., McLay, K., Plumb, B., Davis, J., Clee, C., Oliver, K., Clark, R., Riddle, C., Elliot, D., Threadgold, G., Harden, G., Ware, D., Begum, S., Mortimore, B., Kerry, G., Heath, P., Phillimore, B., Tracey, A., Corby, N., Dunn, M., Johnson, C., Wood, J., Clark, S., Pelan, S., Griffiths, G., Smith, M., Glithero, R., Howden, P., Barker, N., Lloyd, C., Stevens, C., Harley, J., Holt, K., Panagiotidis, G., Lovell, J., Beasley, H., Henderson, C., Gordon, D., Auger, K., Wright, D., Collins, J., Raisen, C., Dyer, L., Leung, K., Robertson, L., Ambridge, K., Leongamornlert, D., McGuire, S., Gilderthorp, R., Griffiths, C., Manthravadi, D., Nichol, S., Barker, G., Whitehead, S., Kay, M., Brown, J., Murnane, C., Gray, E., Humphries, M., Sycamore, N., Barker, D., Saunders, D., Wallis, J., Babbage, A., Hammond, S., Mashreghi-Mohammadi, M., Barr, L., Martin, S., Wray, P., Ellington, A., Matthews, N., Ellwood, M., Woodmansey, R., Clark, G., Cooper, J., Tromans, A., Grafham, D., Skuce, C., Pandian, R., Andrews, R., Harrison, E., Kimberley, A., Garnett, J., Fosker, N., Hall, R., Garner, P., Kelly, D., Bird, C., Palmer, S., Gehring, I., Berger, A., Dooley, C. M., Ersan-Ürün, Z., Eser, C., Geiger, H., Geisler, M., Karotki, L., Kirn, A., Konantz, J., Konantz, M., Oberländer, M., Rudolph-Geiger, S., Teucke, M., Lanz, C., Raddatz, G., Osoegawa, K., Zhu, B., Rapp, A., Widaa, S., Langford, C., Yang, F., Schuster, S.C., Carter, N.P., Harrow, J., Ning, Z., Herrero, J., Searle, S.M., Enright, A., Geisler, R., Plasterk, R.H., Lee, C., Westerfield, M., de Jong, P.J., Zon, L.I., Postlethwait, J.H., Nüsslein-Volhard, C., Hubbard, T.J., Roest Crollius, H., Rogers, J., Stemple, D.L., 2013. The zebrafish reference genome sequence and its relationship to the human genome. Nature 496, 498–503.

Ganley, I.G., Lam du, H., Wang, J., Ding, X., Chen, S., Jiang, X., 2009. ULK1.ATG13. FIP200 complex mediates mTOR signaling and is essential for autophagy. J. Biol. Chem. 284, 12297–12305.

Gao, H., Zhang, L., Zhu, A., Liu, X., Wang, T., Wan, M., Yang, X., Zhang, Y., Zhang, Y., 2020. Metabolic profiling of nuciferine *in vivo* and *in vitro*. J. Agric. Food Chem.

Heinz, S., Benner, C., Spann, N., Bertolino, E., Lin, Y.C., Laslo, P., Cheng, J.X., Murre, C., Singh, H., Glass, C.K., 2010. Simple combinations of lineage-determining transcription factors prime cis-regulatory elements required for macrophage and B cell identities. Mol. Cell 38, 576–589.

Chongqing Traditional Chinese Medicine Hospital, 1957. Preliminary report on the clinical efficacy of chuanlian slices in the treatment of 1,327 cases of ascariasis. J. Tradit. Chinese Med. 142–144.

Hu, W., Nevzorova, Y.A., Haas, U., Moro, N., Sicinski, P., Geng, Y., Barbacid, M., Trautwein, C., Liedtke, C., 2014. Concurrent deletion of cyclin E1 and cyclin-dependent kinase 2 in hepatocytes inhibits DNA replication and liver regeneration in mice. Hepatology 59, 651–660.

Huang da, W., Sherman, B.T., Lempicki, R.A., 2009. Systematic and integrative analysis of large gene lists using DAVID bioinformatics resources. Nat. Protoc. 4, 44–57.

Jones, J.D., Monroe, J., Koutmou, K.S., 2020. A molecular-level perspective on the frequency, distribution, and consequences of messenger RNA modifications. Wiley Interdiscip. Rev. RNa 11, e1586.

Joosten, R.P., Long, F., Murshudov, G.N., Perrakis, A., 2014. The PDB_REDO server for macromolecular structure model optimization. IUCrJ. 1, 213–220.

Juretschke, T., Beli, P., 2021. Causes and consequences of DNA damage-induced autophagy. Matrix. Biol. 100-101, 39–53.

Kadumuri, R.V., Janga, S.C., 2018. Epitranscriptomic code and its alterations in human disease. Trends Mol. Med. 24, 886–903.

Ke, P.Y., 2019. Diverse functions of autophagy in liver physiology and liver diseases. Int. J. Mol. Sci. 20.

Kong, H., Chandel, N.S., 2018. Regulation of redox balance in cancer and T cells. J. Biol. Chem. 293, 7499–7507.

König, J., Zarnack, K., Rot, G., Curk, T., Kayikci, M., Zupan, B., Turner, D.J., Luscombe, N.M., Ule, J., 2010. iCLIP reveals the function of hnRNP particles in splicing at individual nucleotide resolution. Nat. Struct. Mol. Biol. 17, 909–915.

Kumar, A.V., Mills, J., Lapierre, L.R., 2022. Selective autophagy receptor p62/SQSTM1, a pivotal player in stress and aging. Front. Cell Dev. Biol. 10, 793328.

Lanz, M.C., Dibitetto, D., Smolka, M.B., 2019. DNA damage kinase signaling: checkpoint and repair at 30 years. EMBO J. 38, e101801.

Li, Q., Cheng, T., Wang, Y., Bryant, S.H., 2010. PubChem as a public resource for drug discovery. Drug Discov. Today 15, 1052–1057.

Li, Shao., 2021. Network Pharmacology Evaluation Method Guidance - draft. World J. Tradit. Chinese Med. 7 (1), 146–154.

Lill, M.A., Danielson, M.L., 2011. Computer-aided drug design platform using PyMOL. J. Comput. Aided Mol. Des. 25, 13–19.

Lin, X., Zhang, J., Wu, Z., Shi, Y., Chen, M., Li, M., Hu, H., Tian, K., Lv, X., Li, C., Liu, Y., Gao, X., Yang, Q., Chen, K., Zhu, A., 2024. Involvement of autophagy in mesaconitine-induced neurotoxicity in HT22 cells revealed through integrated transcriptomic, proteomic, and m6A epitranscriptomic profiling. Front. Pharmacol. 15, 1393717.

Linse, J.B., Hub, J.S., 2021. Three- and four-site models for heavy water: SPC/E-HW, TIP3P-HW, and TIP4P/2005-HW. J. Chem. Phys. 154, 194501.

Lopes, C.T., Franz, M., Kazi, F., Donaldson, S.L., Morris, Q., Bader, G.D., 2010. Cytoscape web: an interactive web-based network browser. Bioinformatics 26, 2347–2348.

Lu, X., Ji, C., Tong, W., Lian, X., Wu, Y., Fan, X., Gao, Y., 2016. Integrated analysis of microRNA and mRNA expression profiles highlights the complex and dynamic behavior of toosendanin-induced liver injury in mice. Sci. Rep. 6, 34225.

Luo, L., Liang, Y., Fu, Y., Liang, Z., Zheng, J., Lan, J., Shen, F., Huang, Z., 2022. Toosendanin induces hepatocyte damage by inhibiting autophagic flux *via* TFEB-mediated lysosomal dysfunction. Pharmaceuticals 15.

Maier, J.A., Martinez, C., Kasavajhala, K., Wickstrom, L., Hauser, K.E., Simmerling, C., 2015. ff14SB: improving the accuracy of protein side chain and backbone parameters from ff99SB. J. Chem. Theory Comput. 11, 3696–3713.

Meng, J., Cui, X., Rao, M.K., Chen, Y., Huang, Y., 2013. Exome-based analysis for RNA epigenome sequencing data. Bioinformatics 29, 1565–1567.

Niida, H., Nakanishi, M., 2006. DNA damage checkpoints in mammals. Mutagenesis 21, 3–9.

Otsuji, R., Hata, N., Yamamoto, H., Kuga, D., Hatae, R., Sangatsuda, Y., Fujioka, Y., Noguchi, N., Sako, A., Togao, O., Yoshitake, T., Nakamizo, A., Mizoguchi, M., Yoshimoto, K., 2024. Hemizygous deletion of cyclin-dependent kinase inhibitor 2A/B with p16 immuno-negative and methylthioadenosine phosphorylase retention predicts poor prognosis in IDH-mutant adult glioma. Neurooncol. Adv. 6, vdae069.

Preston, G., Emmerzaal, T., Kirdar, F., Schrader, L., Henckens, M., Morava, E., Kozicz, T., 2020. Cerebellar mitochondrial dysfunction and concomitant multi-system fatty acid oxidation defects are sufficient to discriminate PTSD-like and resilient male mice. Brain Behav. Immun. Health 6, 100104.

Qi, S.Y., Jin, R.M., Liu, H.J., Huang, Y.W., 2008. Mechanism studies on hepatotoxicity of rats induced by fructus toosendan. Zhongguo Zhong Yao Za Zhi. 33, 2045–2047.

Ramírez, F., Ryan, D.P., Grüning, B., Bhardwaj, V., Kilpert, F., Richter, A.S., Heyne, S., Dündar, F., Manke, T., 2016. deepTools2: a next generation web server for deep-sequencing data analysis. Nucleic Acids Res. 44, W160–W165.

Ru, J., Li, P., Wang, J., Zhou, W., Li, B., Huang, C., Li, P., Guo, Z., Tao, W., Yang, Y., Xu, X., Li, Y., Wang, Y., Yang, L., 2014. TCMSP: a database of systems pharmacology for drug discovery from herbal medicines. J. Cheminform. 6, 13.

Shao, S., Li, S., Liu, C., Zhang, W., Zhang, Z., Zhu, S., Feng, Y., Pan, Y., 2020. Toosendanin induces apoptosis of MKN-45 human gastric cancer cells partly through miR-23a-3p-mediated downregulation of BCL2. Mol. Med. Rep. 22, 1793–1802.

Smith, M.L., Chen, I.T., Zhan, Q., Bae, I., Chen, C.Y., Gilmer, T.M., Kastan, M.B., O'Connor, P.M., Fornace Jr., A.J., 1994. Interaction of the p53-regulated protein Gadd45 with proliferating cell nuclear antigen. Science (New York, N.Y.) 266, 1376–1380.

Song, J., Park, C., Cabanting, F.E.B., Jun, YW., 2024. Therapeutic upregulation of DNA repair pathways: strategies and small molecule activators. RSC Med. Chem. 15 (12), 3970–3977, 11.

Szklarczyk, D., Kirsch, R., Koutrouli, M., Nastou, K., Mehryary, F., Hachilif, R., Gable, A. L., Fang, T., Doncheva, N.T., Pyysalo, S., Bork, P., Jensen, L.J., von Mering, C., 2023. The STRING database in 2023: protein-protein association networks and functional enrichment analyses for any sequenced genome of interest. Nucleic Acids Res. 51, D638–d646.

Tang, Y., Chen, K., Song, B., Ma, J., Wu, X., Xu, Q., Wei, Z., Su, J., Liu, G., Rong, R., Lu, Z., de Magalhães, J.P., Rigden, D.J., Meng, J., 2021. m6A-Atlas: a comprehensive knowledgebase for unraveling the N6-methyladenosine (m6A) epitranscriptome. Nucleic Acids Res. 49, D134–d143.

van Hameren, G., Campbell, G., Deck, M., Berthelot, J., Gautier, B., Quintana, P., Chrast, R., Tricaud, N., 2019. *In vivo* real-time dynamics of ATP and ROS production in axonal mitochondria show decoupling in mouse models of peripheral neuropathies. Acta Neuropathol. Commun. 7, 86.

Wang, G., Feng, C.C., Chu, S.J., Zhang, R., Lu, Y.M., Zhu, J.S., Zhang, J., 2015. Toosendanin inhibits growth and induces apoptosis in colorectal cancer cells through suppression of AKT/GSK-3β/β-catenin pathway. Int. J. Oncol. 47, 1767–1774.

Wang, G., Li, L., Li, Y., Zhang, L.H., 2023. Toosendanin reduces cisplatin resistance in ovarian cancer through modulating the miR-195/ERK/β-catenin pathway. Phytomedicine 109, 154571.

Winterbourn, C.C., 2020. Hydrogen peroxide reactivity and specificity in thiol-based cell signalling. Biochem. Soc. Trans. 48, 745–754.

Wu, Q., Gao, X., Lin, Y., Wu, C., Zhang, J., Chen, M., Wen, J., Wu, Y., Tian, K., Bao, W., Sun, P., Zhu, A., 2024. Integrating epigenetics, proteomics, and metabolomics to reveal the involvement of Wnt/β-catenin signaling pathway in oridonin-induced reproductive toxicity. Toxics 12.

Wu, Y., Chen, X., Bao, W., Hong, X., Li, C., Lu, J., Zhang, D., Zhu, A., 2022. Effect of humantenine on mRNA m6A modification and expression in human colon cancer cell line HCT116. Genes 13.

Yahata, T., Takanashi, T., Muguruma, Y., Ibrahim, A.A., Matsuzawa, H., Uno, T., Sheng, Y., Onizuka, M., Ito, M., Kato, S., Ando, K., 2011. Accumulation of oxidative DNA damage restricts the self-renewal capacity of human hematopoietic stem cells. Blood 118, 2941–2950.

Yan, X., Zhuo, Y., Bian, X., Li, J., Zhang, Y., Ma, L., Lu, G., Guo, M.Q., Wu, J.L., Li, N., 2019. Integrated proteomics, biological functional assessments, and metabolomics reveal toosendanin-induced hepatic energy metabolic disorders. Chem. Res. Toxicol. 32, 668–680.

Yang, T., Huo, J., Xu, R., Zhang, Y., 2021. Synergistic effect of toosendanin and regorafenib against cell proliferation and migration by regulating WWOX signaling pathway in hepatocellular carcinoma. PhytOther Res. 35, 4567–4578.

Yang, X., Liu, C., Li, Z., Wen, J., He, J., Lu, Y., Liao, Q., Wang, T., Tang, H., Yang, X., Zeng, L., 2024. Paclitaxel hyperthermia suppresses gastric cancer migration through MiR-183-5p/PPP2CA/AKT/GSK3β/β-catenin axis. J. Cancer Res. Clin. Oncol. 150, 416.

Yu, X., Yu, H., Lu, Y., Zhang, C., Wang, H., 2024. Genetic and epigenetic variations underlying flavonoid divergence in Beihua and Sijihua honeysuckles. Epigenet. Insights 17, e002.

Zhang, J., Yang, F., Mei, X., Yang, R., Lu, B., Wang, Z., Ji, L., 2022. Toosendanin and isotoosendanin suppress triple-negative breast cancer growth *via* inducing necrosis, apoptosis and autophagy. Chem. Biol. Interact. 351, 109739.

Zhang, Y., Tang, C.-P., Ke, C.-Q., Yao, S., Ye, Y., 2010. Limonoids and triterpenoids from the stem bark of *melia toosendan*. J. Nat. Prod. 73, 664–668.

Zhao, Y., Shi, Y., Shen, H., Xie, W., 2020. m(6)A-binding proteins: the emerging crucial performers in epigenetics. J. Hematol. Oncol. 13, 35.

Zheng, J., Ji, C., Lu, X., Tong, W., Fan, X., Gao, Y., 2015. Integrated expression profiles of mRNA and microRNA in the liver of *Fructus Meliae Toosendan* water extract injured mice. Front. Pharmacol. 6, 236.

Zoete, V., Daina, A., Bovigny, C., Michielin, O., 2016. SwissSimilarity: a web tool for low to ultra high throughput ligand-based virtual screening. J. Chem. Inf. Model. 56, 1399–1404.

Zorov, D.B., Juhaszova, M., Sollott, S.J., 2014. Mitochondrial reactive oxygen species (ROS) and ROS-induced ROS release. Physiol. Rev. 94, 909–950.